molecular pharmaceutics

Article

Synthesis and bioevaluation of novel 18FDG-conjugated 2-nitroimidazole derivatives for tumor-hypoxia imaging

Xianteng Yang, Fan Wang, Hua Zhu, Zhi Yang, and TaiWei Chu

Mol. Pharmaceutics, **Just Accepted Manuscript** • DOI: 10.1021/acs.molpharmaceut.9b00075 • Publication Date (Web): 09 Apr 2019

Just Accepted

ACS Publications

is published by the American Chemical Society. 1155 Sixteenth Street N.W., Washington, DC 20036

Graphic abstract

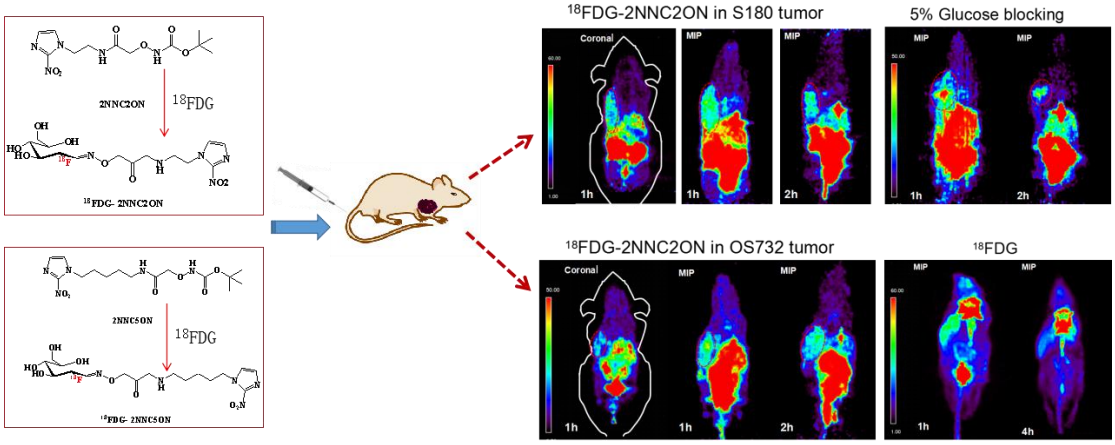

Headline: Two new 2-nitroimidazole derivatives conjugated with ^{18}FDG, ^{18}FDG-2NNC2ON and ^{18}FDG-2NNC5ON, was successfully designed, synthesized and bioevaluated. ^{18}FDG-2NNC2ON has potential as a hypoxic imaging agent for clinical application.

Synthesis and bioevaluation of novel ^{18}FDG-conjugated 2-nitroimidazole derivatives for tumor hypoxia imaging

Xianteng Yang[1,2#], Fan Wang[3#], Hua Zhu[4], Zhi Yang[4*], Taiwei Chu[3*]

1. Guizhou University School of Medicine, Guiyang, Guizhou, 550025, China ;

2. Department of Orthopaedics, Guizhou Provincial People's Hospital, Guiyang, Guizhou, 550002, China;

3. Radiochemistry and Radiation Chemistry Key Laboratory of Fundamental Science, College of Chemistry and Molecular Engineering, Peking University, Beijing 100871, China;

4. Key Laboratory of Carcinogenesis and Translational Research (Ministry of Education/Beijing), Department of Nuclear Medicine, Peking University Cancer Hospital & Institute, Beijing 100142, China.

#: Xianteng Yang and Fan Wang have contributed equally to this work.

* Corresponding author: Yang Zhi, E-mail: pekyz@163.com; Taiwei Chu, E-mail: twchu@pku.edu.cn

Abstract: Hypoxia imaging can guide tumor treatment and monitor changes in hypoxia during treatment. However, there is still no ideal hypoxia imaging agent for clinical applications. In this study, two novel 2-nitromidazole derivatives were synthesized and directly radiolabeled by [^{18}F]FDG in high radiochemical yield and excellent radiochemical purity. Cell experiments, biodistribution and PET imaging studies were also conducted in mice bearing S180 or OS732 tumors. [^{18}F]FDG-2NNC2ON ((2R,3S,4R,E)-2-^{18}F-fluoro-3,4,5,6-tetrahydroxyhexanal O-3-(2-(2-nitro-1H-imidazol-1-yl)ethylamino) -2-oxopropyl oxime) and [^{18}F]FDG-2NNC5ON ((2R,3S,4R,E)-2-^{18}F-fluoro-3,4,5,6 -tetrahydroxyhexanal-O-3-(5-(2-nitro-1H-imidazol-1-yl)pentylamino)-2-oxopropyl oxime) can be

cleared from the blood quickly and specifically target hypoxic tumor cells. The uptake of the probes by hypoxic cells gradually increases with time. After 4 h, the uptake value of [^{18}F]FDG-2NNC2ON in hypoxic cells is 3.2 times higher than that in normoxia cells. In contrast, there is no difference in the uptake of [^{18}F]FDG between hypoxic cells and normoxia cells. Biodistribution results from two tumor models indicate that the uptake values of the two radiotracers in the tumor are higher at 1 h than at 2 and 4 h. At 1 and 2 h, the tumors are clearly observed on the PET images, and the imaging features of [^{18}F]FDG-2NNC5ON and [^{18}F]FDG-2NNC2ON are distinct from those of [^{18}F]FDG. Compared with [^{18}F]FDG-2NNC5ON, [^{18}F]FDG-2NNC2ON has a higher proportion of renal excretion, lower digestive tract uptake and better imaging contrast due to its higher hydrophilicity. At 2 h, [^{18}F]FDG-2NNC2ON shows a good tumor-to-blood (T/B) ratio, tumor-to-muscle ratio based on biodistribution (Bio-T/M ratio), and tumor-to-muscle ratio based on regions of interest on the PET images (ROI-T/M ratio) in the two tumor models (T/B, Bio-T/M and ROI-T/M ratios are 3.2, 2.6 and 3.9 in the S180 tumor model and are 3.4, 4.2 and 4.6 in the OS732 tumor model, respectively). The imaging features visualized with autoradiography mostly coincided with the positive areas of HIF1α staining by immunofluorescence. Meanwhile, the biodistribution study and PET imaging revealed that the uptake of the radiotracers in the tumor cannot be competed by 5% glucose, confirming that [^{18}F]FDG-2NNC2ON targets the hypoxic regions of the tumors instead of targeting tumors through the glucose metabolism pathway. These results suggest that the new 2-nitroimidazole derivative conjugated with [^{18}F]FDG, [^{18}F]FDG-2NNC2ON, has potential as an imaging agent for hypoxia.

Key words: *2-nitroimidazole, [^{18}F]FDG, tumor, hypoxia imaging*

1. Introduction

Hypoxia is a typical feature of solid tumors and one of the main reasons for the failure of tumor-targeted radiotherapy and chemotherapy [1-3]. Therefore, identification of tumor hypoxia is crucial for the treatment of tumors. With the development of molecular imaging technology, there is no doubt that radioactive imaging with a hypoxia-targeted agent has more advantages compared with traditional invasive detection. Hypoxia imaging of tumors by positron emission tomography (PET) can clearly show the hypoxic areas in tumors and improve the clinical efficacy of treatment strategies. However, the hypoxia imaging quality is determined by the performance of the hypoxia imaging agent. So far, there has not been an ideal hypoxia imaging agent used in the clinic yet. It is important to develop a hypoxia-targeted tracer with excellent performance to guide clinical treatment.

Many hypoxia agents have been developed, most of which are based on the nitroimidazole analogues [4]. In particular, 2-nitroimidazole derivatives have been considered to be more suitable for detecting hypoxia because 2-nitroimidazole has a lower single electron reduction potential (SERP) value and may be more effectively restricted to hypoxic cells [5]. ^{18}F is one of the most important radionuclides for PET imaging, and it causes low amounts of radiation side effect to the human body because of its suitable half-life ($t_{1/2,}$ 109.7 min). Currently, many ^{18}F-labeled 2-nitroimidazole derivatives have been prepared for studying hypoxia in tumors [6-18]. The representative ^{18}F-labeled 2-nitroimidazole derivative is [^{18}F]FMISO [9], which has been used to detect tumor clinically. However, [^{18}F]FMISO is limited by its drawbacks, such as the low ratio between the radioactivity in the hypoxic tissue and in the background tissue, high lipophilicity, long blood retention time, high radioactivity concentration in the digestive tract; thus, further improvements are required for effective imaging [19]. In an attempt to overcome some of the above drawbacks, second- and third-generation 2-nitroimidazole

radiotracers, such as [^{18}F]FETNIM [20], [^{18}F]EF5 [21], and [^{18}F]HX4 [16], have been developed. However, the qualities of these hypoxic imaging agents are not better than that of [^{18}F]FMISO. Glycosylation is one of the most commonly used modification strategies that can increase the hydrophilicity of the probe, increase the proportion of renal elimination, reduce the physiological uptake of the probe in the digestive system, reduce the clearance of the reticuloendothelial system, accelerate blood clearance, and shorten the time interval between injection of the tracer to imaging. In 1999, Kumar et al [22]. synthesized [^{18}F]FAZA successfully, and the results of the bioevaluation indicated that [^{18}F]FAZA had potential as a hypoxia imaging agent [23]. Patt et al. synthesized [^{18}F]FDG-2-NIm in 2002; [^{18}F]FDG-2-NIm [18] was obtained by the direct coupling of a 2-nitroimidazole derivative to [^{18}F]FDG, but it cannot specifically target the hypoxic region of the tumor and failed to provide tumor images. Recently, Cao et al. synthesized several novel PEG-modified nitroimidazole tracers by rapid click-reactions [6]. Unfortunately, these molecules [6] did not exhibit specific targeting ability for tumor cells in hypoxic conditions, and no images of the hypoxic regions of tumors have been reported. Therefore, ^{18}F-labeled nitroimidazole hypoxia imaging agents are worthy of further study.

For the ^{18}F-labeled hypoxic imaging agents, an efficient, rapid, and convenient method is needed to overcome the challenges of short half-lives and harsh conditions. Compared with direct introduction of ^{18}F, the strategy for labeling small molecules with ^{18}F may be a more convenient and efficient method. [^{18}F]FDG (2-^{18}F-fluoro-2-deoxy-D-glucose) has been widely used in clinic for PET imaging, and it is an ideal small-molecule for indirect ^{18}F-labeling. Some researchers have reported a method for the radiosynthesis of ^{18}F-labeled peptides using [^{18}F]FDG by chemoselective oxime formation [24-27]. At the same time, ^{18}F-fluorine labeling of a tracer with [^{18}F]FDG as an auxiliary group can achieve effects similar to those of glycosylation modifications. It is hypothesized that this method

can improve synthesis efficiency, increase probe hydrophilicity, overcome some challenges of nitroimidazole reagents, and enhance the contrast and usefulness of PET images. However, this hypothesis has not been investigated yet.

Herein, two novel aminooxy-functionalized 2-nitroimidazole derivatives were synthesized and directly radiolabeled by [^{18}F]FDG (**Figure 1**). Then, the radiotracers were evaluated by corresponding experiments to evaluate their potential for hypoxia imaging.

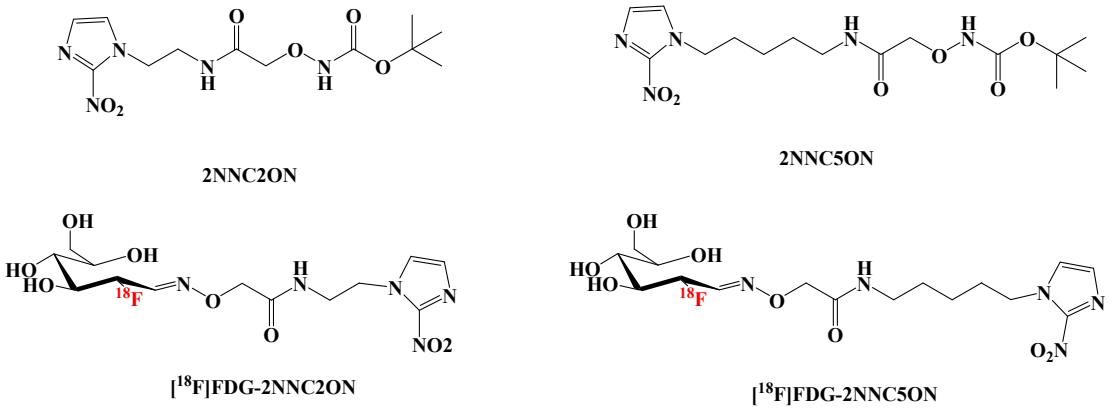

Figure 1. The structures of the compounds.

2. Materials and methods

All chemical reagents and solvents were purchased from commercial suppliers and were used directly without any further purification. [^{18}F]FDG was obtained from the Peking University School of Oncology and Beijing Institute for Cancer Research. FDG was purchased from Shanghai Yuanye Biotechnology Co., Ltd (Shanghai, China). DMEM, fetal bovine serum (FBS), and human serum albumin (HSA) were purchased from Invitrogen (CA, USA). Rabbit anti-HIF-1 alpha (bs-0737R) was purchased from Bioss (Beijing, China). Dye-conjugated goat anti-rabbit IgG (Alexa Fluor® 488, ab150077) was purchased from Abcam (Shanghai, China). Human osteosarcoma OS732 and mouse S180 cells were provided by the Cancer Hospital, Chinese Academy of Medical Sciences (Beijing,

China). The ^{1}H NMR and ^{13}C NMR spectra were obtained on a Bruker spectrometer (Bruker, Germany). Mass spectrometry (including high resolution mass spectra, HRMS) was acquired on a Fourier-transform ion cyclotron resonance mass spectrometer (Bruker, Germany). IR spectra were obtained on Fourier-transform infrared spectrometer (ThermoFisher, USA). The radiochemical yield (RCY) and radiochemical purity (RCP) were determined by a radio-HPLC system (Agilent Technologies 1200 series of high-performance liquid chromatography systems, California, USA) equipped with a UV absorption detector and a B-Fc-1000 HPLC radioactivity detector (Bioscan, USA). The radioactivity of the samples was measured by FH463A- Automatic Scaler (Nuclear Instrument Factory of Beijing, China) and FJ374 well gamma detector (Nuclear Instrument Factory of Beijing, China). A JPS-605-dissolved oxygen meter was purchased from REX Instrument Factory of Shanghai Precision & Scientific Instrument Co., LTD. (Shanghai, China). For autoradiography, the compounds were exposed overnight to a high-sensitivity imaging film (BAS-SR2025, Fuji Photo Film, Japan). PET imaging was conducted by a Super Argus PET/CT system (Sedecal, Spain).

2.1 Chemical synthesis

The compounds **1-10** were prepared according to the method reported with a little modification [24, 28-30], and synthetic procedures are shown in the **Scheme 1.** The detailed procedures and corresponding characterization data of the other compounds are provided in the **Supporting Information,** except for compound **7**-**10**.

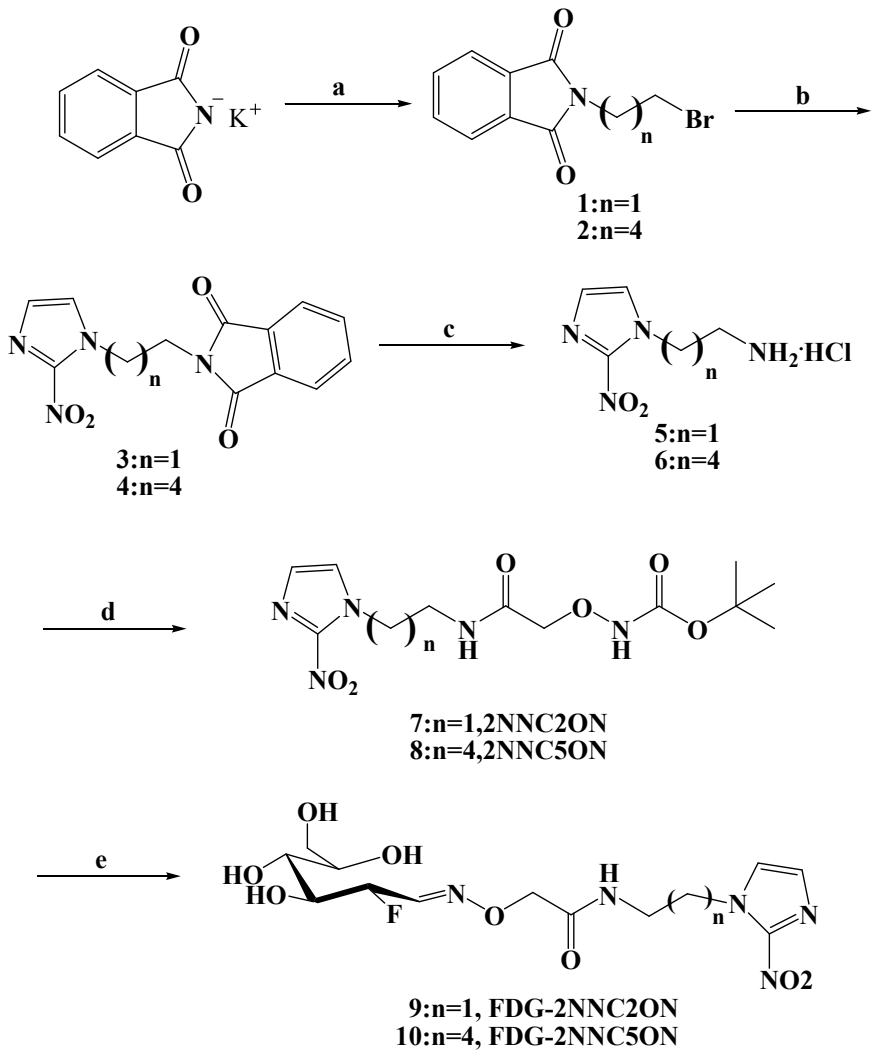

Scheme 1. The synthesis of compounds **1-10**. Reagents and conditions: (a) $BrCH_2CH_2Br$ or $BrCH_2CH_2CH_2CH_2CH_2Br$, K_2CO_3, MeCN, Reflux, 24 h; (b) 2-nitroimidazole, K_2CO_3, MeCN, Reflux; (c) $NH_2NH_2{\cdot}H_2O$, ethanol, Reflux, $HCl{\cdot}Et_2O$; (d) Boc-Aoa, DCM, Et_3N, EDCl, HOBt; and (e) FDG, 0.1M HCl, MeCN.

Synthesis of compound 7 (2NNC2ON, tert-butyl 2-(2-(2-nitro-1H-imidazol-1-yl)ethylamino)-2-oxoethoxycarbamate). Boc-Aoa (Boc-aminooxy acetic acid, 0.49 g, 2.33 mmol), EDCl (1-ethyl-(3-dimethylaminopropyl)carbodiimide hydrochloride, 0.54 g, 2.8 mmol), HOBt (1-hydroxybenzotriazole hydrate, 0.43 g, 2.8 mmol), and Et_3N (0.71 g, 6.99 mmol) were dissolved in 30 mL DCM. The mixture was stirred for 1 h at 0 °C. Afterwards, compound **5** (0.47 g, 2.44 mmol) was added, and the mixture was stirred overnight at room temperature. Then, the organic phase was washed by 20 mL 1 M HCl, 20 mL saturated sodium bicarbonate solution, and 20 mL saturated saline, consecutively. The organic phase was dried by Na_2SO_4 and evaporated under reduced pressure. The crude product was purified by chromatography (ethyl acetate:petroleum ether = 3:2) to obtain compound **7** as a yellow solid (0.47 g, yield: 61%).

^{1}H NMR (400 MHz, DMSO): δ 10.17 (s, 1H), 8.08 (s, 1H), 7.51 (s, 1H), 7.14 (s, 1H), 4.48 (s, 2H), 4.09 (s, 2H), 3.57 (s, 2H), 1.41 (s, 9H).

^{13}C NMR (101 MHz, $CDCl_3$): δ 169.98, 158.15, 144.75, 128.26, 126.68, 83.62, 76.35, 49.01, 39.04, 28.08.

HRMS-ESI: [M+H$^+$] calculated for $C_{12}H_{20}N_5O_6$, 330.14136; found, 330.14066.

HRMS-ESI: [M+NH_4^+] calculated for $C_{12}H_{23}N_6O_6$, 330.14136; found, 347.16710.

HRMS-ESI: [M+Na$^+$] calculated for $C_{12}H_{19}N_5NaO_6$, 352.12266; found, 352.12330

IR (KBr)/cm^{-1}: 3334(ν NH), 3173(ν NH), 2981, 2928, 1717(ν C=O), 1650(ν C=O), 1556, 1536.1502, 1482, 1459, 1437, 1417, 1396, 1356 ,1279, 1256, 1161, 1117, 1089, 1062, 867, 847, 832, 808, 777, 667 650, 636 594.

Synthesis of compound 8 (2NNC5ON, tert-butyl 2-(5-(2-nitro-1H-imidazol-1-yl) pentylamino)-2-oxoethoxycarbamate). Following a similar procedure to that used in the synthesis of

compound **7**, compound **8** was prepared from compound **6** (1.00 g, 4.26 mmol), Boc-Aoa (0.78 g, 4.06 mmol), EDCl (0.93 g, 4.87 mmol), HOBt (0.75 g, 4.87 mmol), and Et_3N (1.23 g, 12.18 mmol). Compound **8** was a yellow oil (1.24 g, yield: 78.5%).

^{1}H NMR (400 MHz, DMSO): δ 10.31 (s, 1H), 8.02 (s, 1H), 7.68 (s, 1H), 7.18 (s, 1H), 4.37 (t, *J* = 7.3 Hz, 2H), 4.13 (s, 2H), 3.13 (q, *J* = 6.7 Hz, 2H), 1.86 – 1.69 (m, 2H), 1.48 (dd, *J* = 14.5, 7.1 Hz, 2H), 1.41 (s, 9H), 1.32 – 1.25 (m, 2H).

^{13}C NMR (101 MHz, $CDCl_3$): δ 169.06, 158.03, 128.40, 125.99, 83.21, 76.20, 50.14, 38.42, 30.06, 28.67, 28.09, 23.56.

HRMS-ESI: [M+H^+] calculated for $C_{15}H_{26}N_5O_6$, 372.18831; found, 372.18670.

HRMS-ESI: [M+NH_4^+] calculated for $C_{15}H_{29}N_6O_6$, 389.21486; found, 389.21400.

HRMS-ESI: [M+Na^+] calculated for $C_{15}H_{25}N_5NaO_6$, 394.17025; found, 394.16974

IR (KBr)/cm^{-1}: 3297(ν NH), 3115(ν NH), 2975, 2933, 2867, 1721(ν C=O), 1655(ν C=O), 1537, 1484, 1459, 1394, 1358, 1276, 1251, 1161, 1109, 1049, 975, 920, 835, 776, 743, 650, 633, 585, 516.

Synthesis of compound 9 (FDG-2NNC2ON, 2-((((2R,3S,4R,E)-2-fluoro-3,4,5,6-tetrahydroxyhexylidene)amino)oxy)-N-(2-(2-nitro-1H-imidazol-1-yl)ethyl)acetamide).Compound **7** (2.0 mg, 0.006 mmol) and FDG (3.0 mg, 0.016mmol) were dissolved in 2 mL of ACN, then 200 μL of 0.1 M HCl was added. The mixture was heated for 1h at 100 °C. After cooling to room temperature, the solvent was removed under vacuum, and the crude product was analyzed by the HPLC. The analytical conditions were as follows: (A): water (containing 0.1% TFA); and (B) acetonitrile. The elution gradient: 0-10 min 95% A-40% A; and 10-15 min 40%

A-95% A. The product was detected at 254 nm using UV absorption detector. The product was collected (retention time 5.0-6.0 min) and identified by HRMS directly.

HRMS-ESI: [M+H$^+$] calculated for $C_{13}H_{21}FN_5O_8$, 394.13742; found, 394.13708.

HRMS-ESI: [M+Na$^+$] calculated for $C_{13}H_{20}FN_5NaO_8$, 416.11936; found, 416.12971.

Synthesis of compound 10 (FDG-2NNC5ON, 2-((((2R,3S,4R,E)-2-fluoro-3,4,5,6-tetrahydroxyhexylidene)amino)oxy)-N-(5-(2-nitro-1H-imidazol-1-yl)pentyl)acetamide) Following similar synthetic procedure and same separating condition to that used in the synthesis of compound **9**, compound **10** was prepared from compound **8** (2.0 mg, 0.005 mmol), FDG (3.3 mg, 0.018 mmol). The product was detected at 254 nm using UV absorption detector. The product was collected (retention time 7.0-8.0 min) and identified by HRMS directly.

HRMS-ESI: [M+H$^+$] calculated for $C_{16}H_{27}FN_5O_8$, 436.18437; found, 436.18387.

2.2 Radiolabelling and quality control

The radiolabelling of 2NNC2ON and 2NNC5ON was performed according to the method in the literature [24-27], and the reaction routes are shown in **Scheme 2**.

Radiolabeling of 2NNC2ON. The precursor 2NNC2ON (2 mg) was dissolved in 20 μL DMSO, then 140 μL 0.1 M HCl and 200 μL [^{18}F]FDG (180-370 MBq) were added to the solution. The mixture was heated to 130 °C for 30 min. After cooling to room temperature, the mixture volume was diluted to 1 mL with normal saline (0.9% NS) and loaded onto a Sep-pak C18 cartridge. After being eluted with 2 mL 0.9% NS to remove extra [^{18}F]FDG, the product was collected with 0.5 mL ethanol. The collected product was evaporated and dissolved in 0.9% NS for other experiments. The product used in the

blocking experiment was diluted with 5% glucose. The RCY and RCP of the product after purification were measured by radio-HPLC, where the flow rate was maintained at 1 mL/min. The analytical conditions of the radio-HPLC solvents were as follows: (A): water (containing 0.1% TFA); and (B) acetonitrile. The elution gradient: 0-10 min 95% A-40% A; and 10-15 min 40% A-95% A.

Radiolabelling of 2NNC5ON. The radiolabelling, separating, and analytical methods of 2NNC5ON were similar to those of 2NNC2ON.

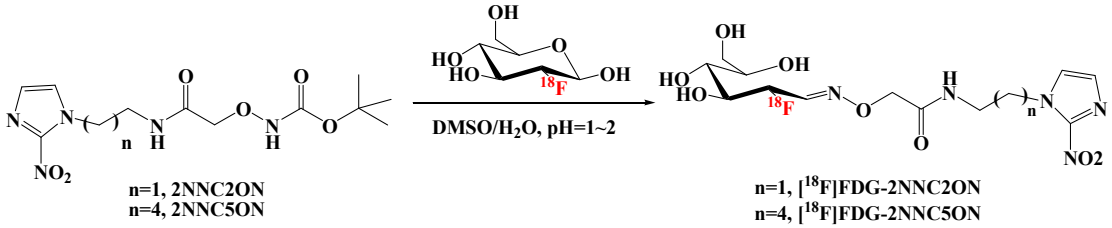

Scheme 2. The radiolabelling of 2NNC2ON and 2NNC5ON.

2.3 *In vitro* experiments

2.3.1 Stability *in vitro*

In vitro stability of the radiolabeled compounds was evaluated in both phosphate buffer solution (PBS, 0.01 M, pH 7.4) and 5% human serum albumin (HSA). Approximately 20 μL of the radiolabeled compound was added to 0.2 mL of PBS or HSA. Then, the mixture was incubated at 37 °C for 4 h. The stability of the radiolabeled compounds in PBS could be directly measured by radio-HPLC. For HSA, aliquots (100 μL) were removed and 200 μL of ethanol was added to precipitate the protein. After centrifugation, the supernatant was filtrated through a 0.22 μm filter, and the filtrate was measured by radio-HPLC.

2.3.2 Partition coefficient

The partition coefficient was measured in a similar method as what was previously reported [31]. In a 5 mL centrifuge tube, 0.1 mL of the radiolabeled compound, 0.9 mL of water and 1 mL of 1-octanol were mixed together. After shaking on a vortex mixer for 5 min at room temperature, the mixture was centrifuged at 5000 rpm for 5 min and allowed to settle for another 10 min. Then, 100 μL of samples were taken from each phase and measured by the gamma counter. The partition coefficient was calculated as follows: P= (the radioactivity of the 1-octanol phase/ the radioactivity of the water phase), and log P was the final expression of the partition coefficient. The experiment was repeated five times. The final results were expressed as the mean ± S.D (standard deviation).

2.3.3 Cell uptake

The S180 cell line was used for the cellular uptake experiments[32]. The cells were diluted to a final concentration of approximately 10^7 cells/mL with PBS (0.01 M, pH 7.4); then the cells (1 mL) were suspended in 20 mL DMEM containing 10% fetal bovine serum at 37 °C with gentle magnetic stirring under hypoxic (95% N_2 + 5% CO_2) and aerobic (95% air +5% CO_2) conditions. After equilibration, 1 mL of the radiolabeled compound (1 MBq) was added. At different time points, five samples were removed from the vial. The 200 μL samples were placed in a 0.5 mL centrifuge tube and centrifuged at 1500 rpm for 5 min. Then, 50 μL of the supernatant was removed from the centrifuge tube and measured as sample A. The residual amount was measured as sample B. The cellular uptake was calculated as follows: %Uptake = (B-3A) / (B+A) ×100%. In this calculation method, the cell volume was ignored. The cell viability was assessed by trypan blue after the experiments, and the cell viability was much higher than 90%. The final results were expressed as the mean ± S.D.

2.4 *In vivo* experiments

2.4.1 Animal model and blood retention in mice

The protocols for all performed animal experiments were approved by the Peking University Cancer Hospital Animal Care and Use Committee. Healthy male Kunming mice were used to assess blood retention, to evaluate *in vivo* stability of the radiolabeled compounds and to establish the S180 tumor model; six-week-old BALB/c nude mice were used to establish the OS732 tumor model, and the specific details are described in the **Supporting Information**.

2.4.2 Stability *in vivo*

In vivo stability of the radiolabeled compounds was also evaluated throught testing urine in animals. The radiolabeled compounds (29.6 MBq, 200 μL, approximately 3.2 mg/mL) were injected into the healthy Kunming mice via the tail vein (n=3). The mice were sacrificed at 3 h postinjection and the urine were collected, filtrated through a 0.22 μm filter and measured by radio-HPLC.

2.4.3 Biodistribution

The radiolabeled compounds (1 MBq, 200 μL, approximately 108 μg/mL) were injected into the S180 or OS732 tumor-bearing mice via the tail vein (n=4). For the competition study, 1 MBq (200 μL) of the radiolabeled compounds diluted with 5% glucose (GS) were injected into mice bearing S180 tumors (n=4). The mice were sacrificed at 1 h, 1 h-competition, 2 h, and 4 h postinjection. After washing, the organs and tissues of interest were collected, weighed and measured for activity on a gamma counter. The results were expressed as percent injected dose per gram of tissue (%ID/g). The final results were expressed as the mean ± S.D.

2.4.4 Micro-PET imaging

The radiolabeled compounds (29.6 MBq, 200 μL, 3.2 mg/mL) were injected into S180 or OS732 tumor-bearing mice. For glucose-competition imaging, a glucose-diluted tracer was injected into S180 tumor-bearing mice. After the injection, the mice were anesthetized with 2.5% isoflurane and maintained under 1.5% isoflurane throughout the imaging experiment. Then, the mice were placed in the prone position and fixed on a micro-PET scanner (Sedecal, Spain). Micro-PET imaging was performed at the indicated time points (1 h, 1 h-competition and 2 h). The parameters for obtaining PET images were as follows: 80 mm diameter transaxial FOV, 900-1200 s PET acquisition time, and OSEM 3D reconstruction iterative algorithms with random and attenuation corrections. At the same time, a semi-quantitative region of interest (ROI) was sketched on the PET image.

2.5 Pathological examination

To verify the expression and distribution of HIF1α in tumor tissues, immunohistochemistry and immunofluorescence were performed at the end of imaging, and the details are provided in the **Supporting Information.**

2.6 Autoradiography of [^{18}F]FDG-2NNC2ON for tissue hypoxia

Tumor specimens of the S180 cell line were selected for autoradiographic analysis. A 30 μm thick slice of the rapidly frozen tumor sample was dried at 40 °C by air and then exposed overnight on a high-sensitivity imaging film (BAS-SR2025, Fuji Photo Film, Japan). The autoradiographic images were analyzed with a computerized imaging analysis system (FLA5100, Fuji Medical System, Stanford, CT, USA) and compared with the immunofluorescently stained image.

2.7 Statistical Analysis

Quantitative data are described as the mean ± S.D. Significant differences between the two sets of data were determined by one-way analysis of variance. SPSS 21.0 software (IBM, Armonk, NY, USA) was used for the statistical analysis. When the P value was <0.05, it was considered statistically significant.

3. Results

3.1 Chemical synthesis and radiolabelling

The compounds **7-8** were synthesized *via* 4 steps from 2-nitroimidazole, and the reaction equations are shown in **Scheme 1**. Products **7-8** were identified by ^{1}H NMR spectra, ^{13}C NMR spectra, HRMS-ESI, and IR ; the results indicate that the target precursors were successfully synthesized, and the corresponding details are provided in the **Supporting Information**. The cold reference compounds **9-10** were also prepared and identified by the HRMS-ESI to certify the identity of the corresponding radiolabeled compounds according to the reaction described in **Scheme 1.**

The RCY and RCP of the products were measured by radio-HPLC. As shown in **Figure 2**, the retention time of [^{18}F]FDG is 3.1 min, while the retention times of [^{18}F]FDG-2NNC2ON and [^{18}F]FDG-2NNC5ON are 6.1 min and 8.1 min, respectively. The RCY of [^{18}F]FDG-2NNC2ON and [^{18}F]FDG-2NNC5ON are 57.6 ± 8.1% and 59.5 ± 9.5% (n=5), respectively. After purification, the RCP of the products are higher than 99%, and the specific activity of [^{18}F]FDG-2NNC2ON and [^{18}F]FDG-2NNC5ON are about 51.8-106.6 and 53.6-110.1 MBq/mg (n=5). Compared with the corresponding cold reference compounds, the retention times of FDG-2NNC2ON and FDG-2NNC5ON are 5.6 min and 7.4 min respectively, which are close with that of the [^{18}F]FDG-2NNC2ON and

[^{18}F]FDG-2NNC5ON. The results indicate that the structures of radiolabeled compounds are proposed structures.

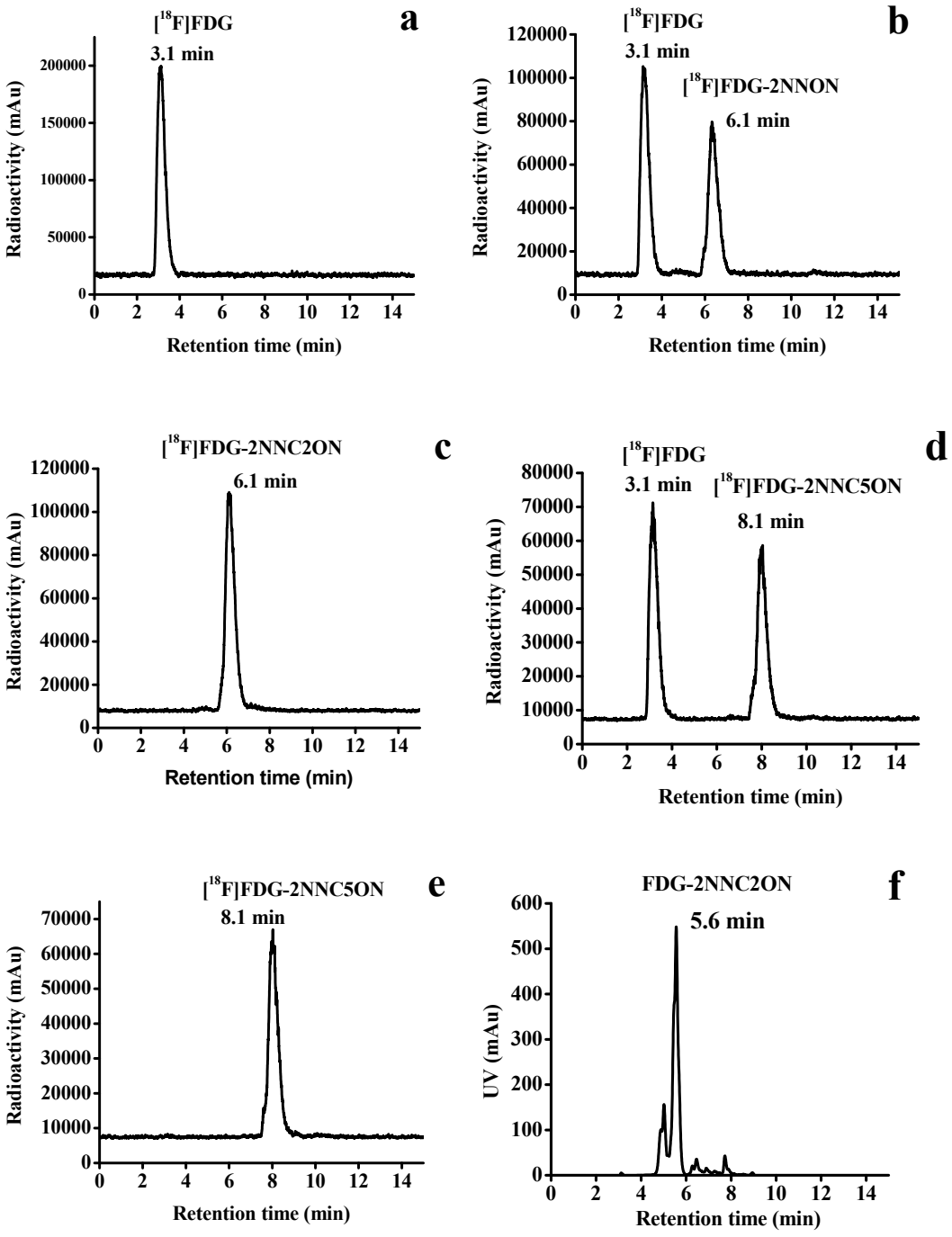

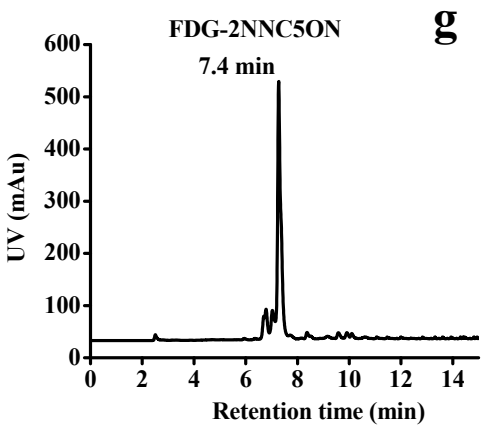

Figure 2 Radio-HPLC chromatograms of [^{18}F]FDG and the [^{18}F]FDG-labeled compounds and UV chromatograms of FDG-2NNC2ON and FDG-2NNC5ON. (a) [^{18}F]FDG; (b) [^{18}F]FDG-2NNC2ON before purification; (c) [^{18}F]FDG- 2NNC2ON after purification; (d) [^{18}F]FDG-2NNC5ON before purification;(e) [^{18}F]FDG-2NNC5ON after purification; (f) the UV chromatogram of FDG-2NNC2ON at 254 nm; and (g) the UV chromatogram of FDG-2NNC5ON at 254 nm.

3.2 Stability

As shown in **Figure 3 a-d**, the RCP of the labeled compounds is still above 99%, which indicates that the compounds are stable for over 3h in urine and over 4 h at 37 ºC in PBS or HSA; this result suggests that the compounds have high stability *in vitro* and *in vivo*.

3.3 *In vitro* experiments

Partition coefficients. The log P values of [^{18}F]FDG-2NNC2ON and [^{18}F]FDG-2NNC5ON are -1.93±0.02 and -1.25±0.03, respectively. The results show that the two compounds are hydrophilic, which may be related to the OH group of FDG.

Cellular uptake experiments. The cellular uptake of [^{18}F]FDG, [^{18}F]FDG-2NNC2ON and [^{18}F]FDG-2NNC5ON in the S180 cell line are shown in **Figure 3 c-e**. At 1 h, the cellular uptake of [^{18}F]FDG-2NNC2ON and [^{18}F]FDG-2NNC5ON in the hypoxic cells is clearly more than that in the aerobic cells, and the difference is statistically significant. In the case of hypoxia, the uptake values of

the two probes in the cells gradually increased with time. At 4 h, the uptake of [^{18}F]FDG-2NNC2ON in the hypoxic cells is 3.2 times higher than that in the aerobic cells, and the uptake of [^{18}F]FDG-2NNC5ON in the hypoxic cells is 2.4 times higher than that in the aerobic cells. In addition, the cellular uptake of [^{18}F]FDG is similar in both hypoxic conditions and aerobic conditions. The results of the *in vitro* cell experiments indicate that [^{18}F]FDG-2NNC2ON and [^{18}F]FDG-2NNC5ON have obvious hypoxic selectivity.

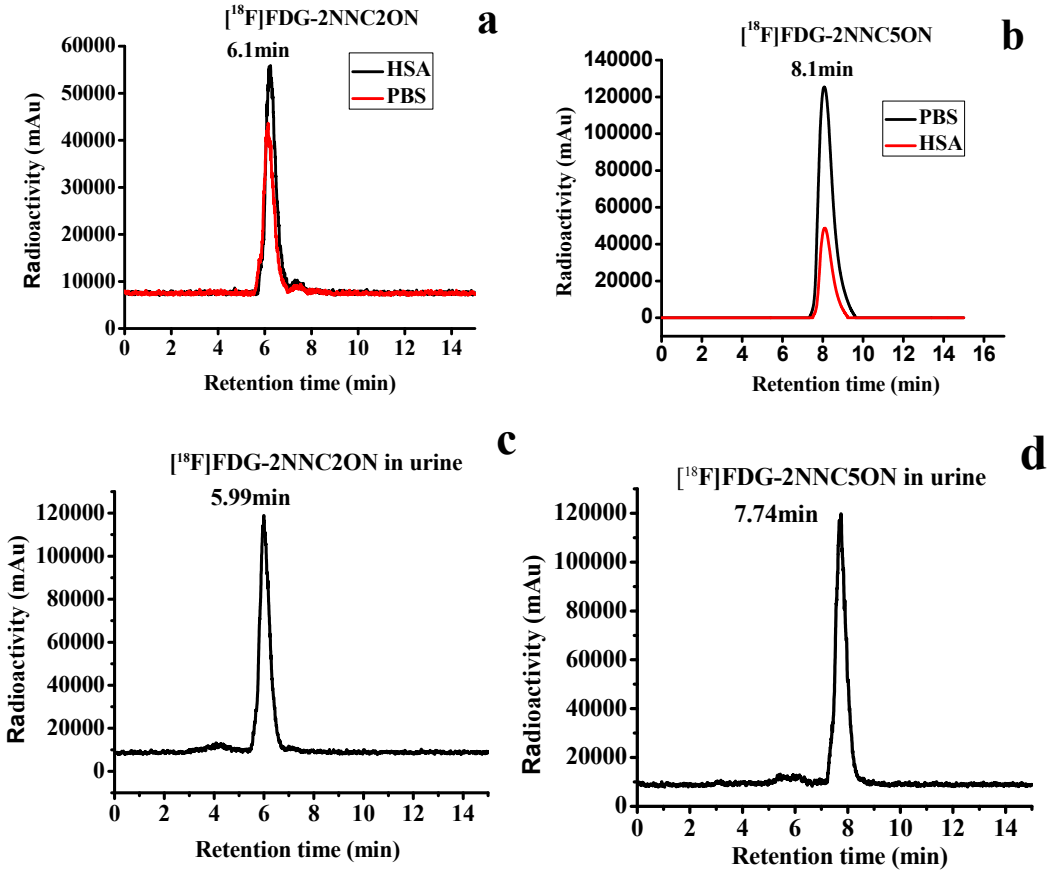

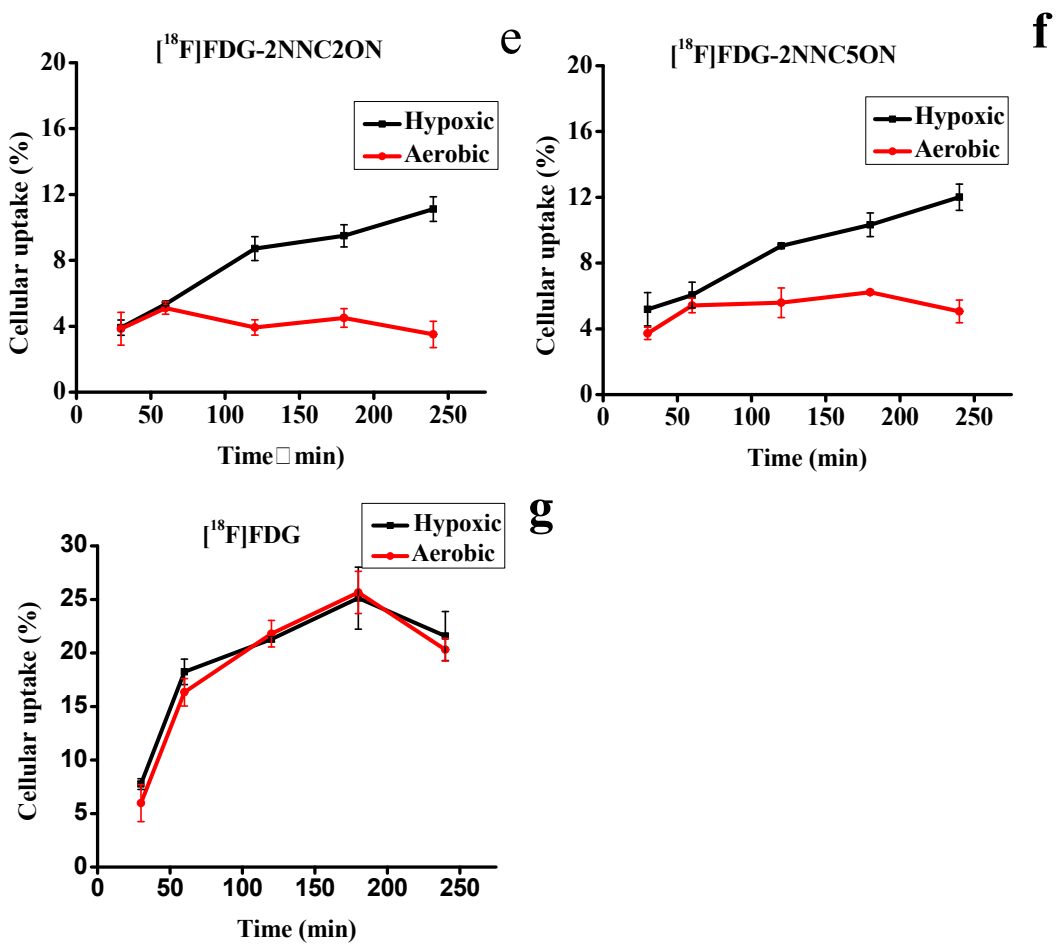

Figure 3 a-b. The RCP of [^{18}F]FDG-2NNC2ON and [^{18}F]DG-2NNC5ON after 4 h at 37 ºC in PBS and 5% HSA. (a) [^{18}F]FDG-2NNC2ON; (b) [^{18}F]FDG-2NNC5ON. **Figure 3 c-d.** The RCP of [^{18}F]FDG-2NNC2ON and [^{18}F]DG-2NNC5ON in urine after 3 h injection. (c) [^{18}F]FDG-2NNC2ON; (d) [^{18}F]FDG-2NNC5ON. **Figure 3 e-g.** The cellular uptake of [^{18}F]FDG-2NNC2ON, and [^{18}F]FDG-2NNC5ON and [^{18}F]FDG in S180 cell lines.

3. 4 *In vivo* experiments

3.4.1 Blood retention in mice

As shown in the **Supporting Information Figure S1**, the radioactivity of the two compounds in the blood rises rapidly and gets eliminates quickly. The results show that the blood retention of [^{18}F]FDG-2NNC2ON and [^{18}F]FDG-2NNC5ON follows the typical blood retention pattern of small

molecule compounds. The curves are fitted with a two-compartment model. The fitted equations of [^{18}F]FDG-2NNC2ON and [^{18}F]FDG-2NNC5ON are $y=20.92 \times e^{-0.23t}+0.78 \times e^{-0.01t}$ ($R^2=0.92$) and $y=4.04 \times e^{-0.17t}+0.94 \times e^{-0.009t}$ ($R^2=0.97$), respectively. The half-life of the distribution phase ($T_{1/2\alpha}$) of [^{18}F]FDG-2NNC2ON and [^{18}F]FDG-2NNC5ON are 3.01 and 4.07 min, respectively, while the half-life of the elimination phase ($T_{1/2\beta}$) of each compound are 69.3 and 77.02 min, respectively.

3.4.2 Biodistribution

The biodistribution results of the two radiotracers in mice bearing S180 tumors and bearing OS732 tumors are shown in **Figure 4**, and the details are described in the **Supporting Information Table S1-4,** respectively. The intestine and liver have the highest uptake values, but the uptake values of the radiotracers in all organs are very low, which suggests that most of inject dose has been eliminated from the urinary system and partly excreted from the hepato-intestinal system. At 1 h, the uptakes values of [^{18}F]FDG-2NNC2ON are 0.4±0.1 %ID/g in S180 tumors and 0.3±0.0 %ID/g in OS732 tumor model, and the uptakes values of [^{18}F]FDG-2NNC5ON are 0.3±0.0 %ID/g in S180 tumor model and 0.3±0.1 %ID/g in OS732 tumors. Although the uptake values in the tumor are not high, the blood and muscle uptake values are extremely low, and the radioactive clearance from the blood and muscle is very fast, so the two compounds exhibit high tumor/blood (T/B) and tumor/muscle (T/M) ratios (**Figure 5 g-h**). At 2 h, the T/B and T/M ratios of [^{18}F]FDG-2NNC2ON in the S180 tumor-bearing mouse are 3.2±0.8 and 2.6±0.9 and are 3.4±0.2 and 4.2±0.7 in the OS732 tumor-bearing mice; the T/B and T/M ratios of [^{18}F]FDG-2NNC5ON in the S180 tumor-bearing mouse are 4.7±0.7 and 5.2±1.0, and are 7.3±2.2 and 5.9±1.5 in the OS732 tumor-bearing mice. After co-injection with 5% GS, although the uptake of the radiotracers in the tumor is a little higher than that

without co-injection of 5% GS, the difference is not statistically significant (**Figure 4 a, c**). This result demonstrates that these two radiotracers do not target the tumors through the glucose metabolism pathway. The difference between the uptake values of [^{18}F]FDG-2NNC2ON and [^{18}F]FDG-2NNC5ON in the tumor is not statistically significant (**Figure 4 e**), suggesting that the increased lipophilicity of [^{18}F]FDG-2NNC5ON does not obviously improve tumor uptake. In the kidneys, the uptake value of [^{18}F]FDG-2NNC2ON is higher than that of [^{18}F]FDG-2NNC5ON. However, in the small intestine, the uptake value of [^{18}F]FDG-2NNC2ON is significantly lower than that of [^{18}F]FDG-2NNC5ON (**Figure 4 f**). These results suggest that the proportion of [^{18}F]FDG-2NNC2ON excreted by the kidney is greater than that of [^{18}F]FDG-2NNC5ON because the lipophilicity of [^{18}F]FDG-2NNC5ON is greater than that of [^{18}F]FDG-2NNC2ON.

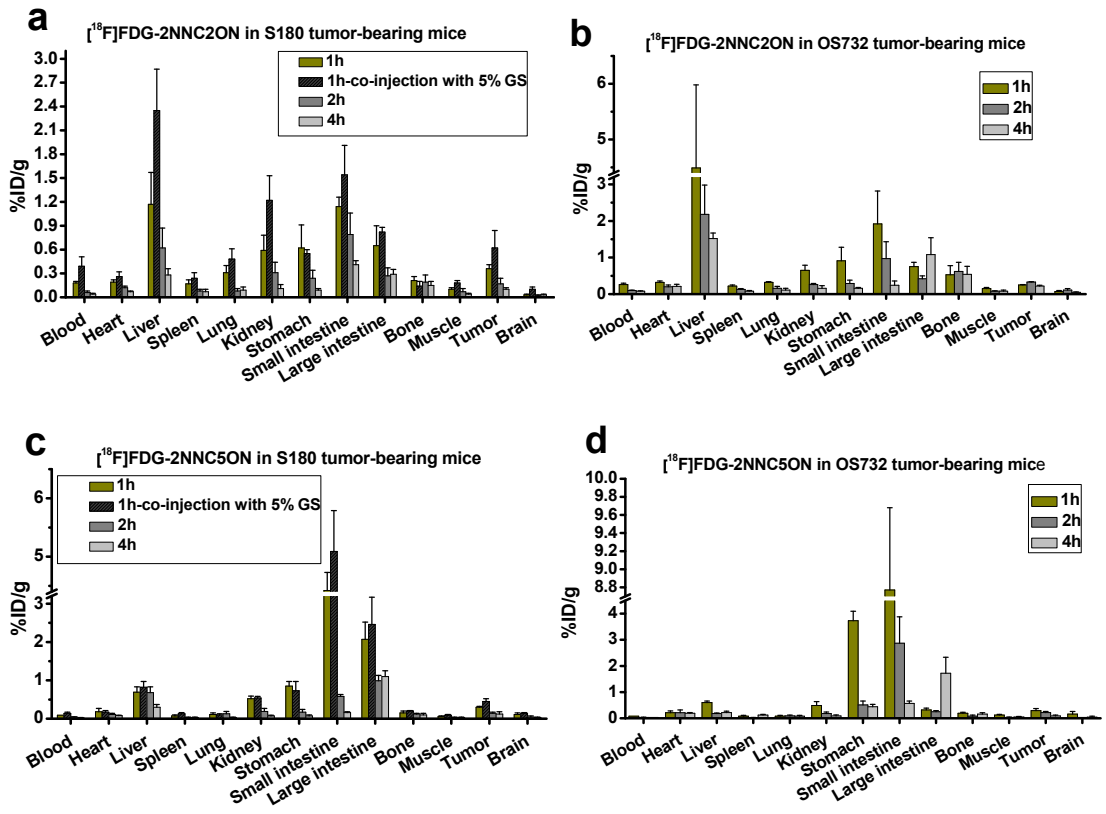

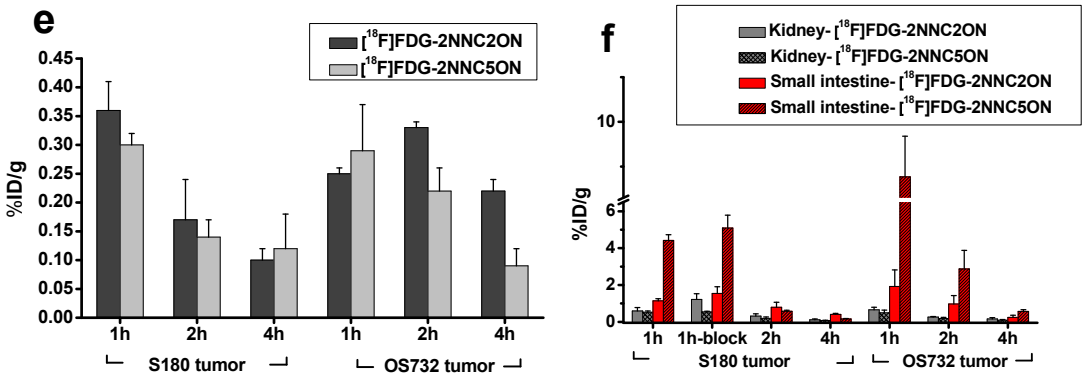

Figure 4: Biodistribution of [^{18}F]FDG-2NNC2ON and [^{18}F]FDG-2NNC5ON in both S180 and OS732 tumor-bearing mice. (a) [^{18}F]FDG-2NNC2ON in S180 tumor-bearing mice; (b) [^{18}F]FDG-2NNC2ON in OS732 tumor-bearing mice; (c) [^{18}F]FDG-2NNC5ON in S180 tumor-bearing mice; (d) [^{18}F]FDG-2NNC5ON in OS732 tumor-bearing mice; (e) Comparison of uptake values of [^{18}F]FDG-2NNC2ON and [^{18}F]FDG-2NNC5ON in tumors. (f) Comparison of uptake values of [^{18}F]FDG-2NNC2ON and [^{18}F]FDG-2NNC5ON in the kidney and small intestine.

3.4.3 Micro-PET imaging

Whole-body PET images were obtained at 1 and 2 h after the injection of the radiotracers, as shown in **Figure 5**. Both the S180 tumor and OS732 tumor could be observed obviously (**Figure 5 a-d**). The intestine has the highest uptake, followed by the liver. The results of the PET imaging are in accordance with the results of the biodistribution. Comparing between [^{18}F]FDG-2NNC2ON and [^{18}F]FDG-2NNC5ON, the PET image of [^{18}F]FDG-2NNC2ON has higher contrast, and the effect of imaging of [^{18}F]FDG-2NNC2ON is better than that of [^{18}F]FDG-2NNC5ON (**Figure 5 a vs c and Figure 5 b vs d**). After competition with 5% GS, the tumor is still clearly visible in the image (**Figure 5 e**). Moreover, to confirm the imaging results of [^{18}F]FDG-2NNC2ON and [^{18}F]FDG-2NNC5ON, imaging was also performed with [^{18}F]FDG in mice bearing OS732 tumors too (**Figure 5 f**). The PET

image with [^{18}F]FDG is significantly different from that of the [^{18}F]FDG-2NNC2ON and [^{18}F]FDG-2NNC because the brain and heart have very significant radioactive tracer uptake. In the S180 tumor model, the tumor to muscle ratio based on ROI (ROI-T/M ratios) of [^{18}F]FDG-2NNC2ON are 2.4 ± 0.3 at 1 h and 3.9 ± 0.1 at 2 h; the ROI-T/M ratios of [^{18}F]FDG-2NNC5ON are 3.4 ± 0.2 at 1 h and 1.5 ± 0.1 at 2 h (**Figure 5 g**). In the human OS732 tumor model, the ROI-T/M ratios of [^{18}F]FDG-2NNC2ON are 3.0 ± 0.4 at 1 h and 4.6 ± 0.6 at 2 h; the ROI-T/M ratios of [^{18}F]FDG-2NNC5ON are 2.8± 0.6 at 1 h and 1.1 ± 0.3 at 2 h (**Figure 5 h**).

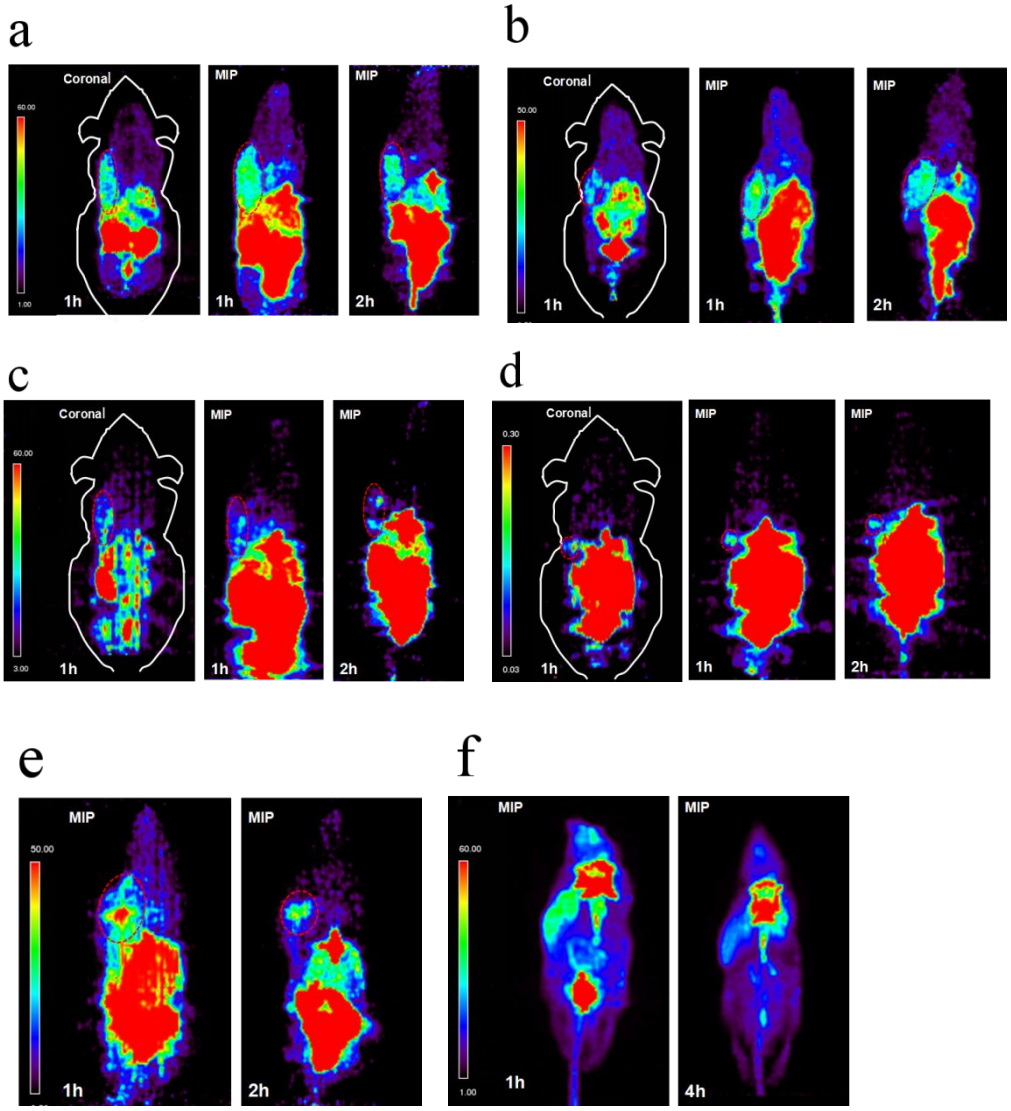

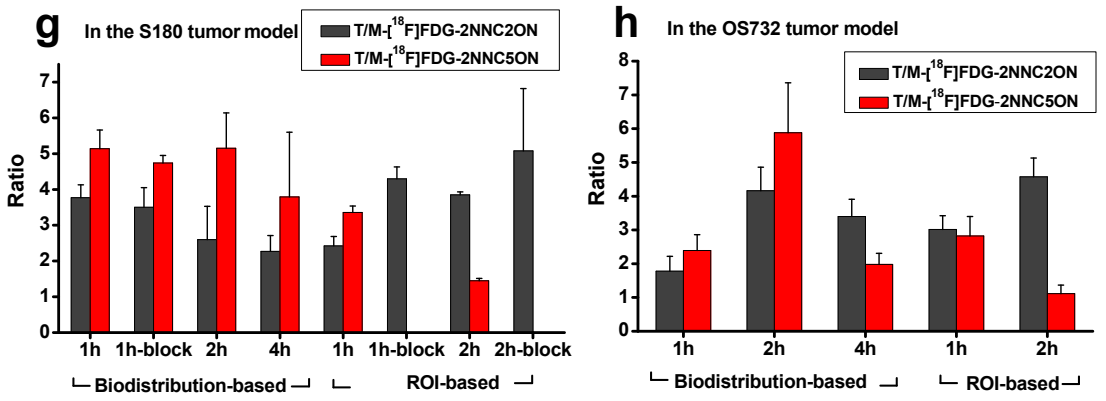

Figure 5. Micro-PET images of [^{18}F]FDG-2NNC2ON and [^{18}F]FDG-2NNC5ON in OS732 and S180 tumor-bearing mice at 1 h and 2 h postinjection. (a) Micro-PET images of [^{18}F]FDG-2NNC2ON in a mouse bearing a S180 tumor; (b) Micro-PET images of [^{18}F]FDG-2NNC2ON in a mouse bearing a human OS732 tumor; The images in figures a-b show the tumor quite clearly. (c) Micro-PET images of [^{18}F]FDG-2NNC5ON in a mouse bearing a S180 tumor; (d) Micro-PET images of [^{18}F]FDG-2NNC5ON in a mouse bearing an OS732 tumor. Figures c-d show that the tumor can be seen, but the contrast of the image is not very high. (e) Micro-PET images of [^{18}F]FDG-2NNC2ON in a mouse bearing a S180 tumor after com with 5% GS, and the tumor is still clearly visible on the image. (f) Micro-PET images of [^{18}F]FDG in a mouse bearing a human OS732 tumor. Figure 5 f shows that the characteristics of the PET image with [^{18}F]FDG are significantly different from those of figures 5 a-e. (g) T/M ratios (both based on biodistribution and ROI) of [^{18}F]FDG-2NNC2ON and [^{18}F]FDG-2NNC5ON in the S180 tumor model. (h) T/M ratios (both based on biodistribution and ROI) of [^{18}F]FDG-2NNC2ON and [^{18}F]FDG-2NNC5ON in the OS732 tumor model.

3.5 Histopathological analysis and autoradiography

The results of the immunohistochemistry and immunofluorescence staining of HIF1α confirm the presence of hypoxia in the S180 and OS732 tumors, as shown in **Figure 6**. From the enlarged pathology image, the expression of HIF1α is observed to be mainly located in the nucleus and cytoplasm. Compared with hematoxylin-eosin staining (HE), the positive area of HIF1α staining is mainly located around the necrotic tumor tissue (**Figure 6 a-c**). In the two adjacent sections of the continuous frozen section, the region positive for HIF1α immunofluorescence staining is generally similar with the imaging area highlighted in autoradiography, suggesting that the radiotracer specifically targets the hypoxic region (Fig 6 c4-5).

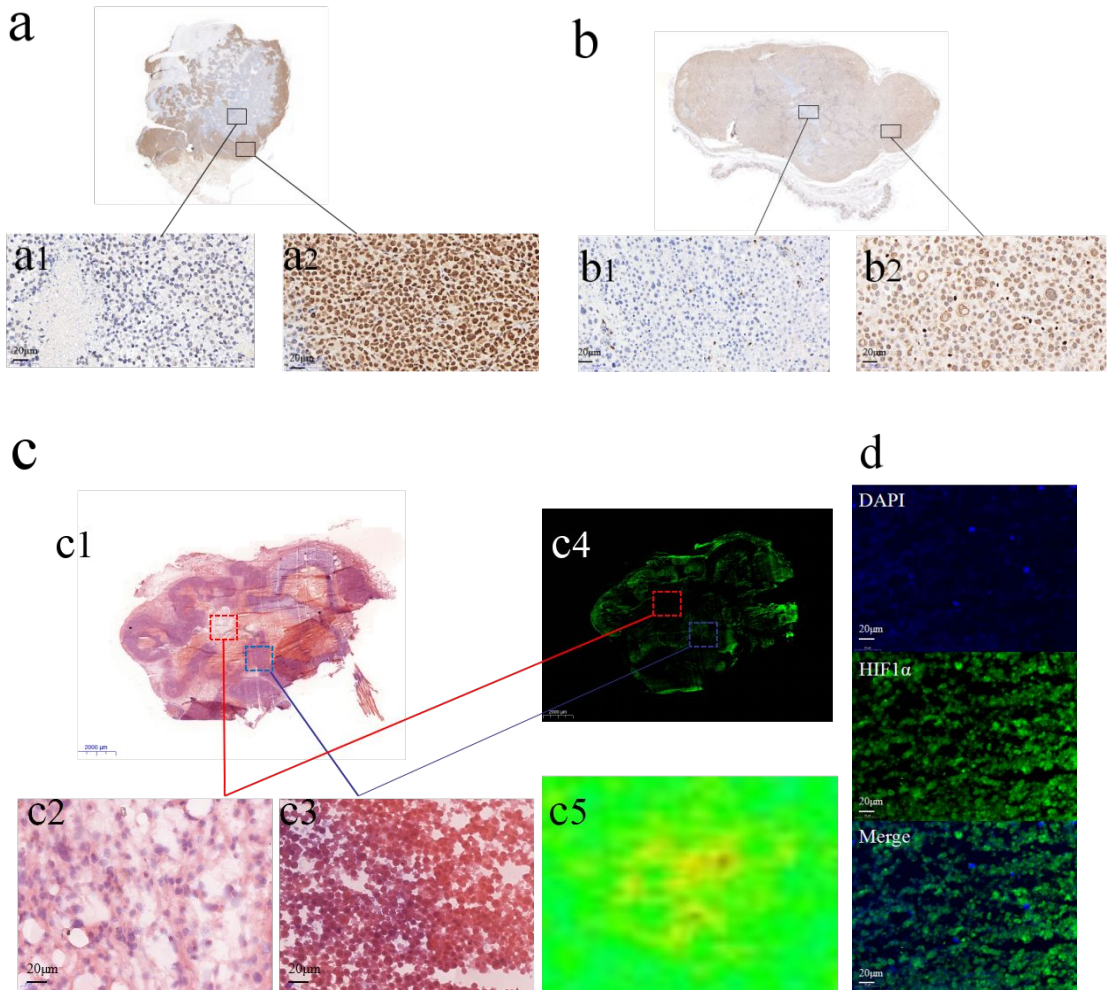

Figure 6. Autoradiography and histopathological analysis images (0.5 × magnification in full landscape image and 30 × magnification in local magnified image). (a, b) Immunohistochemical

staining of S180 (a) and human OS732 (b) tumors. The hypoxic regions are shown in brown. (c) Images from the S180 tumor model of HE staining (c1-3), immunofluorescence staining (c4) to detect HIF1α and autoradiography (c5). (c2) The necrotic area of tumor tissue. (c3) The region around the necrotic tumor tissue. Figures c4 and c5 show that the positive region of HIF1α immunofluorescence staining was mainly consistent with the area highlighted by autoradiography (green area in C4 vs yellow area in C5). HIF1α is expressed in the nucleus and cytoplasm (a1, a2, d).

4. Discussion

In this study, two new nitroimidazole derivatives, 2NNC2ON and 2NNC5ON, were successfully synthesized through 4-step reactions. [^{18}F]FDG-2NNC2ON and [^{18}F]FDG-2NNC5ON could be obtained by one-step reactions within 30 min with a relatively good RCY and are more conveniently synthesized than some ^{18}F-labeled compounds[6,18,23], and show a fast clearance rate in pharmacokinetic studies. Both radiotracers are stable *in vitro*, which meets the quality control standards for clinical applications. In the current study, [^{18}F]FDG-2NNC2ON and [^{18}F]FDG-2NNC5ON demonstrate the ability to specifically target hypoxic cells or hypoxic regions of the tumor, similar to [^{18}F]FAZA [23] and ^{18}FMISO [23]. This ability is crucial because the specific targeting hypoxic regions is a prerequisite for hypoxia imaging agents.

In the *in vivo* experiments, both radiotracers can be taken up by the tumor, and the tumor can be clearly observed on the PET image. Compared to [^{18}F]FDG-2NNC5ON, the PET images with [^{18}F]FDG-2NNC2ON shows the tumor more clearly and has better image contrast. At 2 h, both probes demonstrate excellent tumor-to-background ratios in both tumor models that are comparable to previously reported results in [^{18}F]FMISO [26] and seem even better than what is published in other

reports [6,18]. Interestingly, the T/M and T/B ratios of [^{18}F]FDG-2NNC5ON are higher than those of [^{18}F]FDG-2NNC2ON, but PET imaging of the tumor with [^{18}F]FDG-2NNC5ON is not as good as with [^{18}F]FDG-2NNC2ON. The biodistribution analysis reveals that the uptake of [^{18}F]FDG-2NNC5ON in the intestine is significantly higher than that of [^{18}F]FDG-2NNC2ON, which may be the cause of poorer imaging with [^{18}F]FDG-2NNC5ON.

These studies illustrate that the two compounds (especially [^{18}F]FDG-2NNC2ON) have potential applications in detecting the hypoxic areas of tumors, but the uptake of [^{18}F]FDG-2NNC2ON in the tumor is slightly low because of the high clearance rate *in vivo*. Therefore, to overcome the lower tumor uptake of [^{18}F]FDG-2NNC2ON, a good direction for future research might be prolonging the residence time of [^{18}F]FDG-2NNC2ON.

Moreover, [^{18}F]FDG-2NNC5ON is more lipophilic than [^{18}F]FDG-2NNC2ON due to the extension of its carbon chain. Therefore, in biological distribution and PET imaging studies, [^{18}F]FDG-2NNC2ON demonstrates a higher renal excretion ratio and less digestive tract uptake than [^{18}F]FDG-2NNC5ON, and [^{18}F]FDG-2NNC2ON achieves better tumor imaging. Because of its higher hydrophilicity, [^{18}F]FDG-2NNC2ON diffuses into the tissue from the blood slowly, and its concentration in the blood correspondingly increases in the early stages of drug metabolism, which is more conducive for the uptake of radiotracers by target tissues. These results indicate that the linking group between [^{18}F]FDG and the 2-nitroimidazole derivative has an important effect on the *in vivo* biodistribution of the radiotracers. Therefore, these findings suggest that altering the structure of the linker to develop a hypoxic imaging agent may be another strategy.

5. Conclusion

In summary, we have successfully synthesized two new 2-nitroimidazole hypoxic imaging agents, [^{18}F]FDG-2NNC2ON and [^{18}F]FDG-2NNC5ON, by direct radiolabeling with [^{18}F]FDG. According to the results of the biodistribution, the effects of [^{18}F]FDG-2NNC2ON are better than those of [^{18}F]FDG-2NNC5ON, most likely due to the lower lipophilicity of [^{18}F]FDG-2NNC2ON. The PET imaging qualities of [^{18}F]FDG-2NNC2ON are desirable. These findings suggest that direct radiolabeling with [^{18}F]FDG for the modification of 2-nitroimidazoles is a feasible and convenient method, and a new radiotracer, [^{18}F]FDG-2NNC2ON, has potential as a hypoxic imaging agent for clinical application.

Supporting Information

Blood retention experiments in mice, animal models, pathological examinations, experimental procedures, characterization of the compounds, and the detailed values of the biodistribution are described in the **supporting information**.

Acknowledgements

This work was supported by the National Natural Science Foundation of China (Grant No. 11575010, 21371017, 81571705, 81671733, 81871386, 81560356, and 81871387), Beijing Nova Program (Z171100001117020), Beijing Excellent Talents Funding (2017000021223ZK33), Beijing Municipal Administration of Hospitals-Yangfan Project (ZYLX201816). Beijing Natural Science Foundation, Jing-Jin-Ji special projects for basic research cooperation (H2018206600), Major State Research Development Program of China (2016YFC0100402). The science and Technology Foundation of Guizhou (Grant nos. [2015] 2089 and [2019] 1201). Science and Technology Foundation of Health and Family Planning Commission of Guizhou Province (gzwjkj2018-1-040).

Notes

All authors declare no conflict of interest.

References:

1. Brown, J. M.; Giaccia, A. J. The unique physiology of solid tumors: opportunities (and problems) for cancer therapy. *Cancer Res.* **1998,** 58, (7), 1408-1416.

2. Mckeown, S. R.; Cowen, R. L.; Williams, K. J. Bioreductive Drugs: from Concept to Clinic. *Clin Oncol (R Coll Radiol).* **2007,** 19, (6), 427-442.

3. GRAY, L. H.; CONGER, A. D.; EBERT, M.; HORNSEY, S.; SCOTT, O. C. The concentration of oxygen dissolved in tissues at the time of irradiation as a factor in radiotherapy. *Br J Radiol.* **1953,** 26, (312), 638-648.

4. Nunn, A.; Linder, K.; Strauss, H. W. Nitroimidazoles and imaging hypoxia. *Eur J Nucl Med.* **1995,** 22, (3), 265-280.

5. Ruan, Q.; Zhang, X.; Lin, X,; Duan, X. J.; Zhang, J. B. Novel 99mTc labelled complexes with 2-nitroimidazole isocyanide: design, synthesis and evaluation as potential tumor hypoxia imaging agents. *MEDCHEMCOMM.* **2018**, 9, 988-994.

6. Cao, J. H.; Liu, Y. J.; Zhang, L. F.; Du, F. H.; Zhang, Y.; Xiao, H.; Yao, X. Y.; Shi, S. Y.; Zhu, L.; Kung, H. F.; Qiao, J. P. Synthesis of novel PEG-modified nitroimidazole derivatives via "hot-click" reaction and their biological evaluation as potential PET imaging agent for tumors. *Journal of Radioanalytical & Nuclear Chemistry.* **2017**, 312, 1-14.

7. Yamamoto, F.; Aoki, M.; Furusawa, Y.; Ando, K.; Kuwabara, Y.; Masuda, K.; Sasaki, S.; Maeda, M. Synthesis and evaluation of 4-bromo-1-(3-[18F]fluoropropyl)-2-nitroimidazole with a low energy

LUMO orbital designed as brain hypoxia-targeting imaging agent. *Biol Pharm Bull.* **2002,** 25, (5), 616-621.

8. Yamamoto, F.; Oka, H.; Antoku, S.; Ichiya, Y.; Masuda, K.; Maeda, M. Synthesis and characterization of lipophilic 1-[18F]fluoroalkyl-2-nitroimidazoles for imaging hypoxia. *Biol Pharm Bull.* **1999,** 22, (6), 590-597.

9. Jerabek, P. A.; Patrick, T. B.; Kilbourn, M. R.; Dischino, D. D.; Welch, M. J. Synthesis and biodistribution of 18F-labeled fluoronitroimidazoles: potential in vivo markers of hypoxic tissue. *IInt J Rad Appl Instrum A. 1986, 37, (7), 599-605*.

10. Lin, L. L.; Silvoniemi, A.; Stubbs, J. B.; Rengan, R.; Suilamo, S.; Solin, O.; Divgi, C.; Eskola, O.; Sorger, J. M.; Stabin, M. G.; Kachur, A.; Hahn, S. M.; Grönroos, T. J.; Forsback, S.; Evans, S. M.; Koch, C. J.; Minn, H. Radiation dosimetry and biodistribution of the hypoxia tracer (18)F-EF5 in oncologic patients. *Cancer Biother Radiopharm.* **2012,** 27, (7), 412-419.

11. Evans, S. M.; Kachur, A. V.; Shiue, C. Y.; Hustinx, R.; Jenkins, W. T.; Shive, G. G.; Karp, J. S.; Alavi, A.; Lord, E. M.; Dolbier, W. R. Jr.; Koch, C. J. Noninvasive detection of tumor hypoxia using the 2-nitroimidazole [18F]EF1. *J Nucl Med.* **2000,** 41, (2), 327-336.

12. Wuest, M.; Kumar, P.; Wang, M.; Yang, J.; Jans, H. S.; Wiebe, L. I. In vitro and in vivo evaluation of [(18)F]F-GAZ, a novel oxygen-mimetic azomycin-glucose conjugate, for imaging hypoxic tumor. *Cancer Biother Radiopharm.* **2012,** 27, (8), 473-480.

13. Hu, M.; Xing, L.; Mu, D.; Yang, W.; Yang, G.; Kong, L.; Yu, J. Hypoxia imaging with 18F-fluoroerythronitroimidazole integrated PET/CT and immunohistochemical studies in non-small cell lung cancer. *Clin Nucl Med.* **2013,** 38, (8), 591-596.

14. Mapelli, P.; Incerti, E.; Bettinardi, V.; Conte, G. M.; Fallanca, F.; Bailo, M.; Vuozzo, M.; Callea, M.; Gianolli, L.; Picchio, M. Hypoxia 18 F-FAZA PET/CT imaging in lung cancer and high-grade glioma: open issues in clinical application. *Clinical & Translational Imaging.* **2017**, 5, (4), 389-397.

15. Di, C. G.; Delapaz, R. L.; Brooks, R. A.; Sokoloff, L.; Kornblith, P. L.; Smith, B. H.; Patronas, N. J.; Kufta, C. V.; Kessler, R. M.; Johnston, G. S.; Manning, R. G.; Wolf, A. P. Glucose utilization of cerebral gliomas measured by [18F] fluorodeoxyglucose and positron emission tomography. *NEUROLOGY.* **1982**, 32, (12), 1323-1329.

16. Zegers, C. M. L.; Hoebers, F. J. P.; van Elmpt, W.; Bons, J. A.; Öllers, M. C.; Troost, E. G. C.; Eekers, D.; Balmaekers, L.; Arts-Pechtold, M.; Mottaghy, F. M.; Lambin, P. Evaluation of tumour hypoxia during radiotherapy using [18F]HX4 PET imaging and blood biomarkers in patients with head and neck cancer. *European Journal of Nuclear Medicine and Molecular Imaging.* **2016,** 43, (12), 2139-2146.

17. Mahy, P.; De Bast, M.; Gillart, J.; Labar, D.; Gregoire, V. Detection of tumour hypoxia: comparison between EF5 adducts and [18F]EF3 uptake on an individual mouse tumour basis. *Eur J Nucl Med Mol Imaging.* **2006,** 33, (5), 553-556.

18. Patt, M.; Sorger, D.; Scheunemann, M.; Stocklin, G. Adduct of 2-[18F]FDG and 2-nitroimidazole as a putative radiotracer for the detection of hypoxia with PET: synthesis, in vitro- and in vivo-characterization. *Appl Radiat Isot.* **2002,** 57, (5), 705-712.

19. Bruehlmeier, M.; Roelcke, U.; Schubiger, P. A.; Ametamey, S. M. Assessment of hypoxia and perfusion in human brain tumors using PET with 18F-fluoromisonidazole and 15O-H2O. *Journal of Nuclear Medicine Official Publication Society of Nuclear Medicine.* **2004**, 45, 1851.

20. Gronroos, T.; Bentzen, L.; Marjamaki, P.; Murata, R.; Horsman, M. R.; Keiding, S.; Eskola, O.; Haaparanta, M.; Minn, H.; Solin, O. Comparison of the biodistribution of two hypoxia markers [18 F]FETNIM and [18 F]FMISO in an experimental mammary carcinoma. *Eur J Nucl Med Mol Imaging.* **2004,** 31, (4), 513-20.

21. Komar, G.; Lehtio, K.; Seppanen, M.; Eskola, O.; Levola, H.; Lindholm, P.; Sipila, H.; Seppala, J.; Grenman, R.; Solin, O.; Minn, H. Prognostic value of tumour blood flow, [18 F]EF5 and [18 F]FDG PET/CT imaging in patients with head and neck cancer treated with radiochemotherapy. *Eur J Nucl Med Mol Imaging.* **2014,** 41, (11), 2042-50.

22. Kumar, P.; Stypinski, D.; Xia, H.; McEwan, A. J. B.; Machulla, H. J.; Wiebe, L. I. Fluoroazomycin arabinoside (FAZA): synthesis, 2H and 3H - labelling and preliminary biological evaluation of a novel 2 - nitroimidazole marker of tissue hypoxia. *Journal of Labelled Compounds & Radiopharmaceuticals.* **1999**, 42, 3-16.

23. Sorger, D.; Patt, M.; Kumar, P.; Wiebe, L. I.; Barthel, H.; Seese, A.; Dannenberg, C.; Tannapfel, A.; Kluge, R.; Sabri, O. [18F]Fluoroazomycinarabinofuranoside (18FAZA) and [18F]Fluoromisonidazole (18FMISO): a comparative study of their selective uptake in hypoxic cells and PET imaging in experimental rat tumors. *Nucl Med Biol.* **2003,** 30, (3), 317-326.

24. Namavari, M.; Cheng, Z.; Zhang, R.; De A; Levi, J.; Hoerner, J. K.; Yaghoubi, S. S.; Syud, F. A.; Gambhir, S. S. A novel method for direct site-specific radiolabeling of peptides using [18F]FDG. *Bioconjug Chem.* **2009,** 20, (3), 432-436.

25. Wuest, F.; Hultsch, C.; Berndt, M.; Bergmann, R. Direct labelling of peptides with 2-[18F]fluoro-2-deoxy-d-glucose ([18F]FDG). *Bioorg Med Chem Lett.* **2009,** 19, (18), 5426-5428.

26. Hultsch, C.; Schottelius, M.; Auernheimer, J.; Alke, A.; Wester, H. J. (18)F-Fluoroglucosylation of peptides, exemplified on cyclo(RGDfK). *Eur J Nucl Med Mol Imaging.* **2009,** 36, (9), 1469-74.

27. Şenışık, A. M.; İçhedef, Ç.; Kılçar, A. Y.; Uçar, E.; Arı, K.; Göksoy, D.; Parlak, Y.; Bedriye, E. S. B.; Teksöz, S. One-step conjugation of glycylglycine with [18 F]FDG and a pilot PET imaging study. *Journal of Radioanalytical\s&\snuclear Chemistry.* **2018**, 316, 1-7.

28. Si, W.; Zhang, T.; Zhang, L.; Mei, X.; Dong, M.; Zhang, K.; Ning, J. Design, synthesis and bioactivity of novel phthalimide derivatives as acetylcholinesterase inhibitors. *Bioorg Med Chem Lett.* **2016,** 26, (9), 2380-2.

29. Xu, K.; Wang, F.; Pan, X.; Liu, R.; Ma, J.; Kong, F.; Tang, B. High selectivity imaging of nitroreductase using a near-infrared fluorescence probe in hypoxic tumor. *Chem Commun (Camb).* **2013,** 49, (25), 2554-2556.

30. DENDRINOS, K.; JEONG, J.; HUANG, W.; KALIVRETENOS, A. G. ChemInform Abstract: HOBT Immobilized on Macroporous Polystyrene Beads: A Useful Reagent for the Synthesis of Amides. *CHEM COMMUN.* **1998**, 29, 499-500.

31. Su, Z. F.; Ballinger, J. R.; Rauth, A. M.; Abrams, D. N.; Billinghurst, M. W. A novel amine-dioxime chelator for technetium-99m: synthesis and evaluation of 2-nitroimidazole-containing analogues as markers for hypoxic cells. *Bioconjug Chem.* **2000,** 11, (5), 652-663.

32. Zhang, W.; Zhang, Q.; Chen, Q.; Zhu, H.; Yang, Z.; Chu, T.W. In vitro and in vivo evaluation of a 64 Cu-labeled propylene amine oxime complex as a potential hypoxia imaging agent bearing two 3-nitrotriazole groups. *Journal of Radioanalytical & Nuclear Chemistry.* **2017,** 1(34), 111-118.

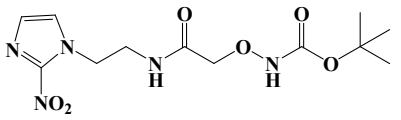

2NNC2ON

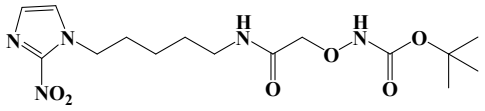

2NNC5ON

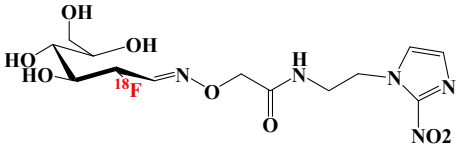

[^{18}F]FDG-2NNC2ON

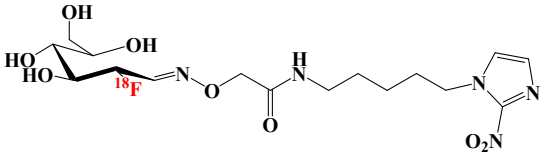

[^{18}F]FDG-2NNC5ON

Figure 1. The structures of the compounds.

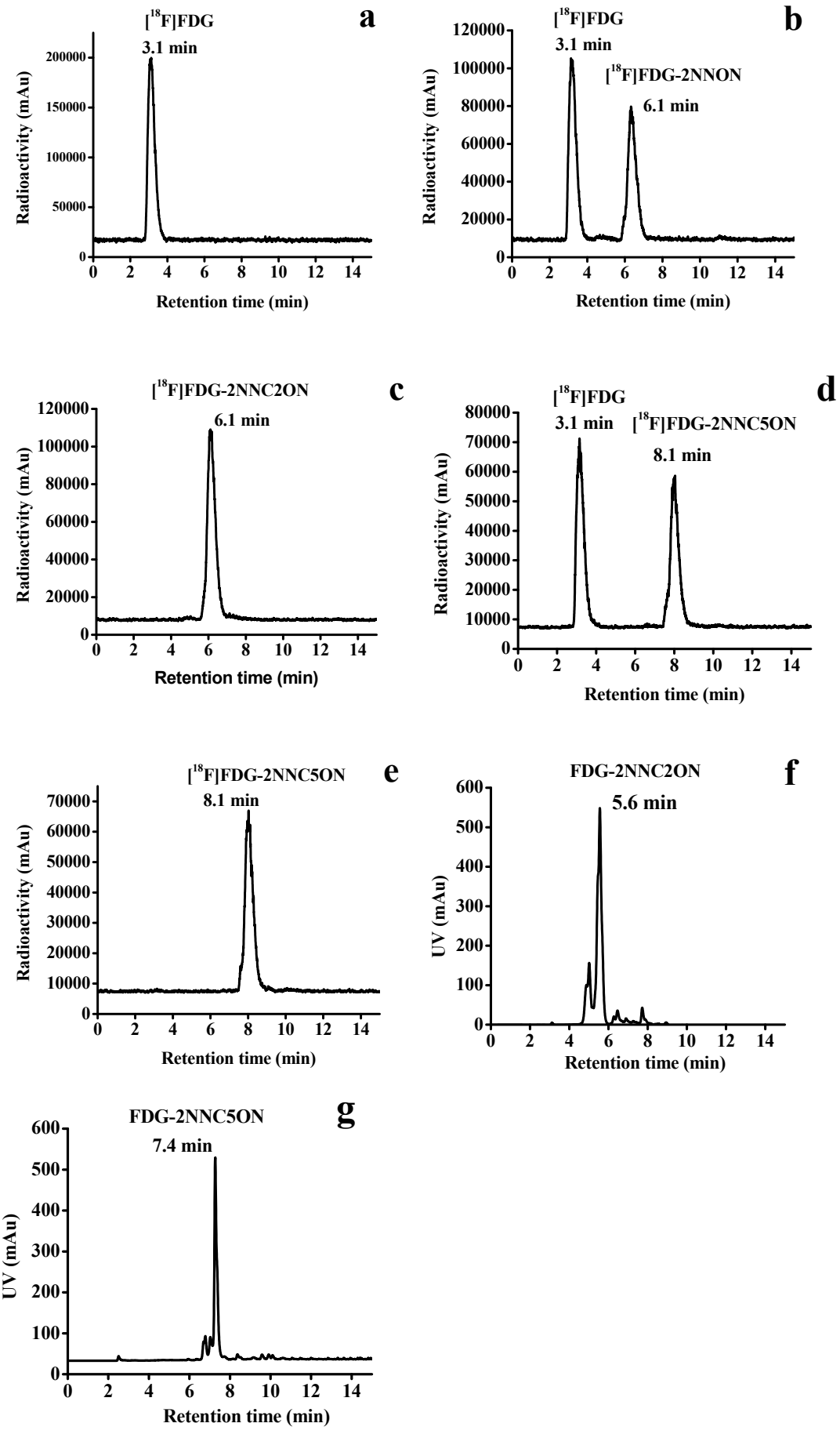
a
[18F]FDG
3.1 min
Radioactivity (mAu)
Retention time (min)
b
[18F]FDG
3.1 min
[18F]FDG-2NNON
6.1 min
Radioactivity (mAu)
Retention time (min)
c
[18F]FDG-2NNC2ON
6.1 min
Radioactivity (mAu)
Retention time (min)
d
[18F]FDG
3.1 min
[18F]FDG-2NNC5ON
8.1 min
Radioactivity (mAu)
Retention time (min)
e
[18F]FDG-2NNC5ON
8.1 min
Radioactivity (mAu)
Retention time (min)
f
FDG-2NNC2ON
5.6 min
UV (mAu)
Retention time (min)
g
FDG-2NNC5ON
7.4 min
UV (mAu)
Retention time (min)

Figure 2 Radio-HPLC chromatograms of [^{18}F]FDG and the [^{18}F]FDG-labeled compounds and UV chromatograms of FDG-2NNC2ON and FDG-2NNC5ON. (a) [^{18}F]FDG; (b) [^{18}F]FDG-2NNC2ON before purification; (c) [^{18}F]FDG- 2NNC2ON after purification; (d) [^{18}F]FDG-2NNC5ON before purification;(e) [^{18}F]FDG-2NNC5ON after purification; (f) the UV chromatogram of FDG-2NNC2ON at 254 nm; and (g) the UV chromatogram of FDG-2NNC5ON at 254 nm.

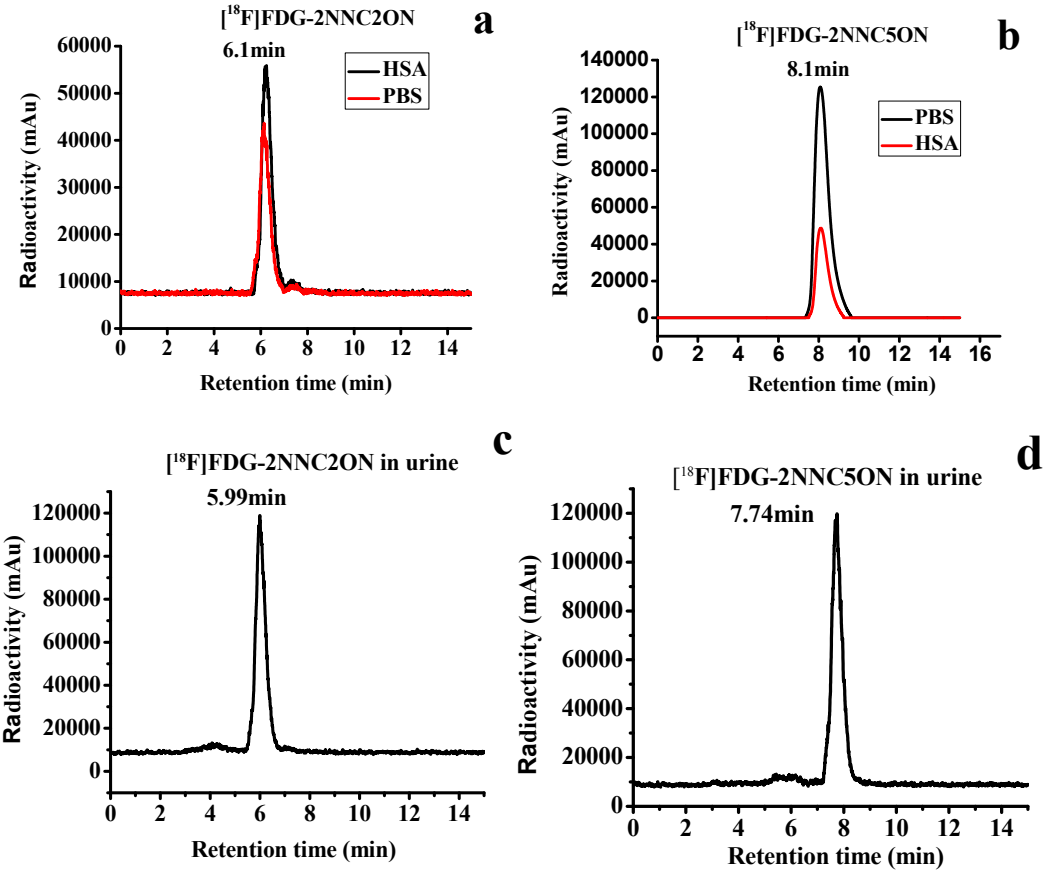

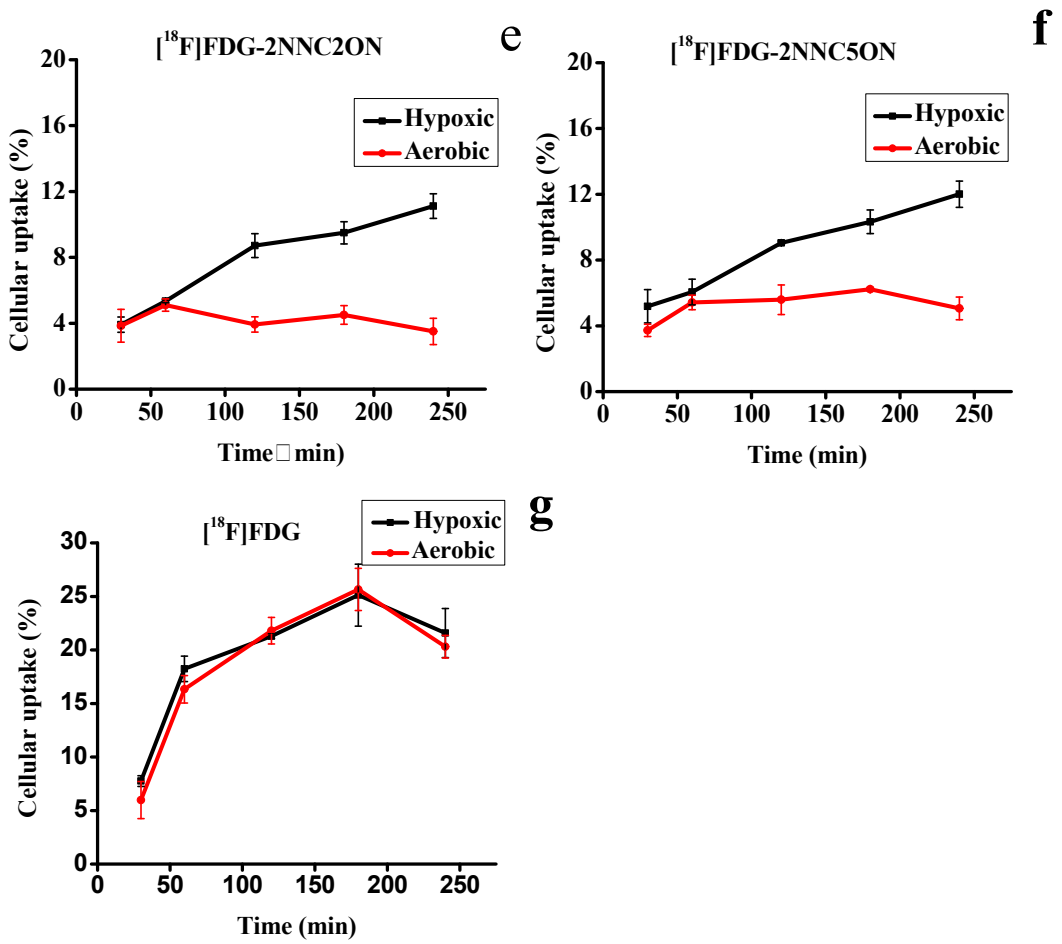

Figure 3 a-b. The RCP of [^{18}F]FDG-2NNC2ON and [^{18}F]DG-2NNC5ON after 4 h at 37 ºC in PBS and 5% HSA. (a) [^{18}F]FDG-2NNC2ON; (b) [^{18}F]FDG-2NNC5ON. **Figure 3 c-d.** The RCP of [^{18}F]FDG-2NNC2ON and [^{18}F]DG-2NNC5ON in urine after 3 h injection. (c) [^{18}F]FDG-2NNC2ON; (d) [^{18}F]FDG-2NNC5ON. **Figure 3 e-g.** The cellular uptake of [^{18}F]FDG-2NNC2ON, and [^{18}F]FDG-2NNC5ON and [^{18}F]FDG in S180 cell lines.

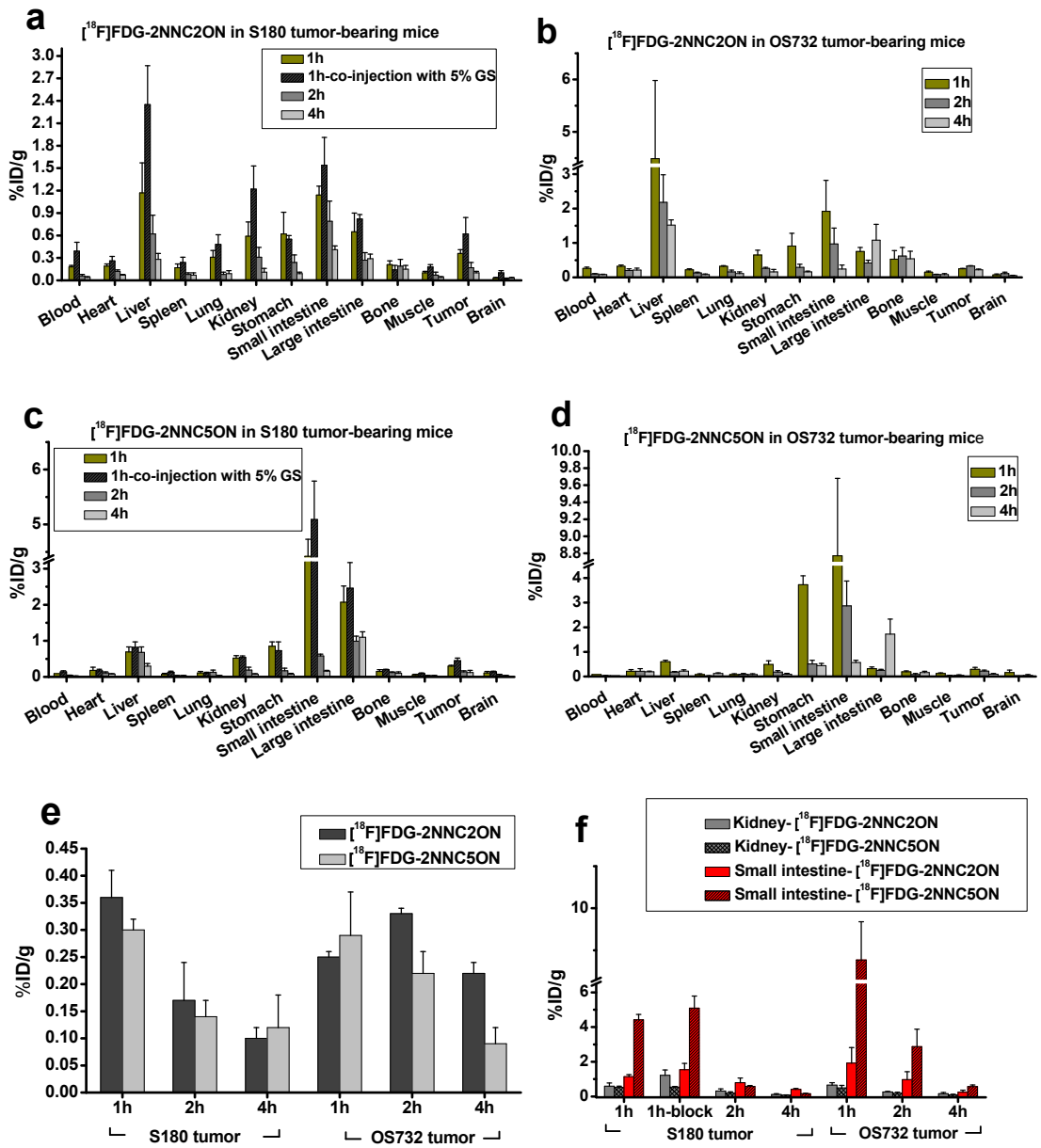

Figure 4: Biodistribution of [^{18}F]FDG-2NNC2ON and [^{18}F]FDG-2NNC5ON in both S180 and OS732 tumor-bearing mice. (a) [^{18}F]FDG-2NNC2ON in S180 tumor-bearing mice; (b) [^{18}F]FDG-2NNC2ON in OS732 tumor-bearing mice; (c) [^{18}F]FDG-2NNC5ON in S180 tumor-bearing mice; (d) [^{18}F]FDG-2NNC5ON in OS732 tumor-bearing mice; (e) Comparison of uptake values of [^{18}F]FDG-2NNC2ON and [^{18}F]FDG-2NNC5ON in tumors. (f) Comparison of uptake values of [^{18}F]FDG-2NNC2ON and [^{18}F]FDG-2NNC5ON in the kidney and small intestine.

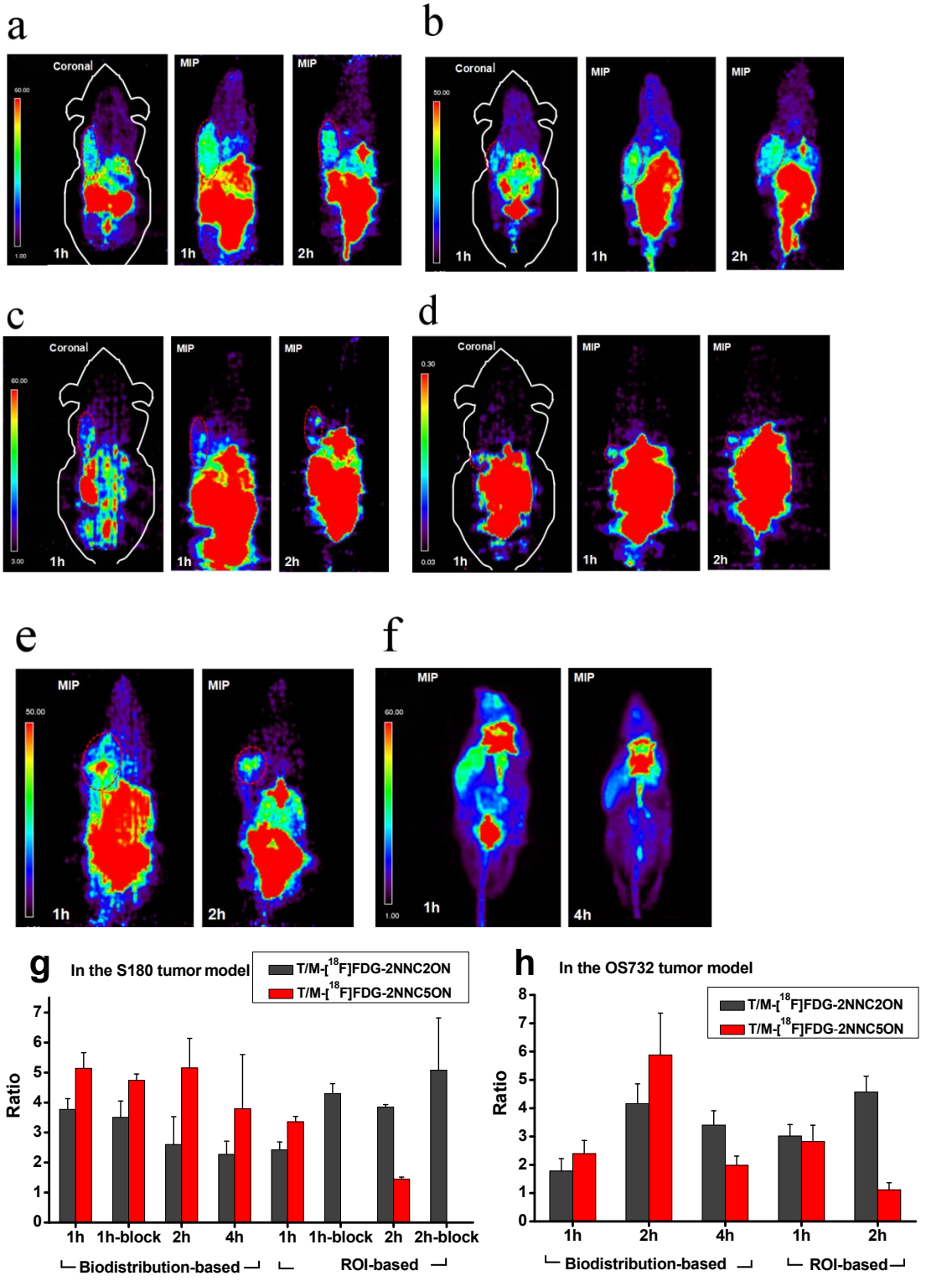

Figure 5. Micro-PET images of [^{18}F]FDG-2NNC2ON and [^{18}F]FDG-2NNC5ON in OS732 and S180 tumor-bearing mice at 1 h and 2 h postinjection. (a) Micro-PET images of [^{18}F]FDG-2NNC2ON in a mouse bearing a S180 tumor; (b) Micro-PET images of [^{18}F]FDG-2NNC2ON in a mouse bearing a human OS732 tumor; The images in figures a-b show the

tumor quite clearly. (c) Micro-PET images of [^{18}F]FDG-2NNC5ON in a mouse bearing a S180 tumor; (d) Micro-PET images of [^{18}F]FDG-2NNC5ON in a mouse bearing an OS732 tumor. Figures c-d show that the tumor can be seen, but the contrast of the image is not very high. (e) Micro-PET images of [^{18}F]FDG-2NNC2ON in a mouse bearing a S180 tumor after com with 5% GS, and the tumor is still clearly visible on the image. (f) Micro-PET images of [^{18}F]FDG in a mouse bearing a human OS732 tumor. Figure 5 f shows that the characteristics of the PET image with [^{18}F]FDG are significantly different from those of figures 5 a-e. (g) T/M ratios (both based on biodistribution and ROI) of [^{18}F]FDG-2NNC2ON and [^{18}F]FDG-2NNC5ON in the S180 tumor model. (h) T/M ratios (both based on biodistribution and ROI) of [^{18}F]FDG-2NNC2ON and [^{18}F]FDG-2NNC5ON in the OS732 tumor model.

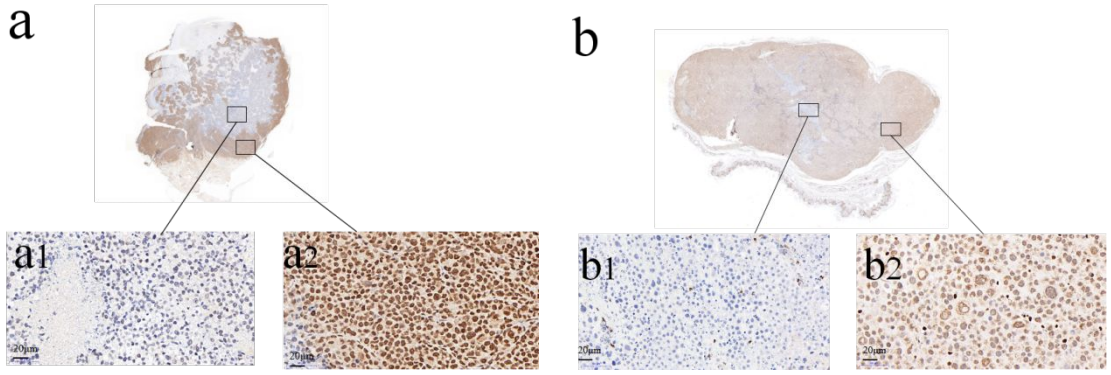

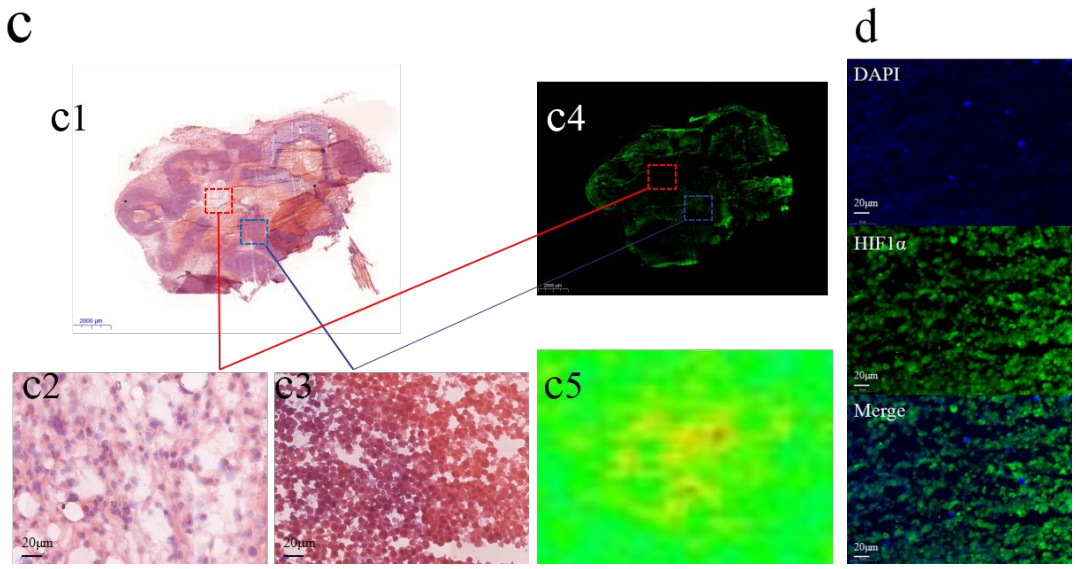

Figure 6. Autoradiography and histopathological analysis images (0.5 × magnification in full landscape image and 30 × magnification in local magnified image). (a, b) Immunohistochemical staining of S180 (a) and human OS732 (b) tumors. The hypoxic regions are shown in brown. (c) Images from the S180 tumor model of HE staining (c1-3), immunofluorescence staining (c4) to detect HIF1α and autoradiography (c5). (c2) The necrotic area of tumor tissue. (c3) The region around the necrotic tumor tissue. Figures c4 and c5 show that the positive region of HIF1α immunofluorescence staining was mainly consistent with the area highlighted by autoradiography (green area in C4 vs yellow area in C5). HIF1α is expressed in the nucleus and cytoplasm (a1, a2, d).